

Studies of magnetization and related properties for hard type-II superconductors

Debjani Karmakar

TPPED, Bhabha Atomic Research Centre, Trombay, Mumbai-400 085, India

E-mail : debjan@magnum.barc.ernet.in

Received 26 May 2005, accepted 17 June 2005

Abstract : Magnetization and the related properties of type-II superconductor are studied in the framework of Critical State Model. We categorized the solvable sample geometries into three possible solvable classes and addressed some unsolved non-trivial problems in each of these three classes. Applications of these problems for realistic experimental situations are discussed. The theoretical results obtained have a good resemblance with the experimental results. A brief discussion of the earlier literature is also presented.

Keywords : Hard type-II superconductors, critical state model demagnetization factor, magnetization, anisotropy, ac susceptibility, higher harmonics.

PACS Nos. : 74.25.Ha, 75.60.Ej

Plan of the Article

1. Introduction

2. Hard type-II superconductors

3. Flux-pinning

4. Critical state models

4.1. Classification of solvable problems

4.2. Propositions of CSM

4.3. Class I problems

4.4. Class II problems

4.5. Class III problems

5. Class I problems : formulation, solution and applications

5.1. Analytical formulation for cylinders

5.1.1. Current density, current shells and flux-fronts

5.1.2. Description of flux-fronts by their conformal map

5.1.3. Surface current density producing uniform interior field

5.1.4. Volume current density

5.1.5. Determination of flux-contours : matrix equations

5.1.6. Numerical scheme

5.2. Magnetization curves

5.3. Results and discussions

5.3.1. Transverse oblique field direction

5.3.2. General field direction

5.3.3. ac susceptibility calculations

5.3.4. Analytical formulation

5.3.5. Results and discussions

5.3.6. Stepwise modification

6. Class II problems

6.1. Critical state model with anisotropic critical current density

6.1.1. Formulation

6.1.2. Elliptic cylinder and elliptic anisotropy

(a) The flux contours

(b) Magnetization curves

(c) Field-dependent critical current density

(d) Summary and discussion

6.2. Studies of order-disorder transitions in weakly pinned vortex matter systems

6.2.1. Formulation for infinite slab geometry

- (a) Field increasing envelope (forward curve)
- (b) Field decreasing envelope (reverse curve)
- (c) Reversal from the field decreasing envelope
- (d) Reversal from the field increasing envelope

6.2.2. Overall characteristics of the order-disorder transitions

7. Class III problems

7.1. Formulation

7.2. Evolution of profiles

- 7.2.1. Non-magnetic initial profile
- 7.2.2. Diamagnetic initial profile
- 7.2.3. Paramagnetic initial profile

7.3. Summary

8. Conclusions

References

1. Introduction

Magnetization measurements on superconductors have constituted a frontline research activity in view of the widespread application of superconductivity in various fields of physics. Such measurements are a powerful tool for the characterization of dissipation phenomena occurring in the mixed state of hard type-II superconductors and can provide an assessment of high field application of these materials. Hard type-II superconductors exhibit irreversibility in their isothermal magnetization. Initially, this irreversibility and resulting magnetization hysteresis was a puzzle, since conventional theories of superconductivity predicted reversible magnetization. For qualitative explanation of the observed hysteresis, Bean [1] proposed a phenomenological model in 1964, which subsequently became known as Bean's Critical State Model (CSM). In its original form, the CSM involved only one parameter, *viz.* the field independent critical current density J_c , below which a superconductor exhibits zero resistance. Later, magnetization hysteresis measurements were used to infer the field dependence of J_c . After the discovery of high T_c materials, magnetization studies began to play a major role for understanding the nature of vortex state in these materials, particularly because it is ideally suited technique for small sized single crystals.

CSM was originally applied to samples in simpler geometries, such as, infinite slab or infinite circular cylinders in parallel geometry corresponding to zero

demagnetization factor (N). Such solutions with a constant J_c assumption provides a qualitative description of the experimental results. It is necessary to incorporate the appropriate field dependence of J_c and the effect of geometry of the sample for quantitative comparison. Solutions for samples having non-zero demagnetization factors are, however, non-trivial and only approximate solutions are available in the literature. Henceforth, to consider realistic situations, solutions of CSM in the non-zero demagnetization factor geometry is needed. Also in the $N = 0$ case, there are some unsolved problems like consideration of intrinsic anisotropy of the material, study of metastability and history dependence in case of order-disorder transition of weakly pinned systems, *etc.* In this Review, we discuss some such unsolved problems for both zero and non-zero demagnetization factor geometry.

The next section starts with some brief description of hard type-II materials and the description of CSM to analyze various observed magnetization properties of such materials. We present a broad classification of the possible sample geometries, which can be solved in the framework of CSM. As a next step, we shall describe our obtained solutions for these possible geometries and their utilization for realistic situations. These solutions of CSM for different applied field directions and sample geometries are useful in understanding the statics and dynamics of vortices under different experimental conditions and, therefore, are valuable for the development of high field superconducting magnet technology.

2. Hard type-II superconductors

Superconductors are characterized by two fundamental length scales *viz.* the London penetration depth (λ) and the coherence length (ξ). By a detailed treatment using Ginzburg Landau theory [2], one can arrive at the definitions of type I and type II superconductors. For type II superconductors, $\kappa = \lambda/\xi > 1/\sqrt{2}$, and the interfacial energy for a planer domain wall between the normal and superconducting region is negative, rendering continuous division of the interface region to maximize the surface to volume ratio of the normal region. This procedure continues until a single quantum of flux Φ_0 is enclosed within the region $\sim \pi\xi^2$. The cylindrical normal core of radius $\sim \xi$, surrounded by the screening currents flowing around to a distance $\sim \lambda$ from the center of the core is termed as a **vortex**. Between the lower and upper critical field, field enters within a type II superconductor in the form of such vortices and this state is known as the **mixed state**. The upper (B_{c1}) and lower (B_{c2}) critical field can be expressed in terms of the fundamental length scales as :

$$B_{c1} = \frac{\Phi_0 \ln \kappa}{4\pi\lambda^2}, \quad (1)$$

$$B_{c2} = \frac{\Phi_0}{2\pi\xi^2}. \quad (2)$$

The thermodynamic critical field $B_c = \sqrt{B_{c1}B_{c2} \ln \kappa}$ is defined as by the difference in the free energy density of the normal and superconducting state. In the absence of any defect (like point defect, grain boundary, color centers, etc.) in the underlying material, the vortices form a regular hexagonal lattice pattern, known as Flux Line Lattice (FLL). A typical magnetization *versus* field measurement results into the curve as shown in Figure 1. For hard type II materials, under reversal of the applied magnetic field, magnetization hysteresis is present due to the pinning of the vortices at the defect sites. In the next section, the effects of pinning on the flux line lattice will be discussed.

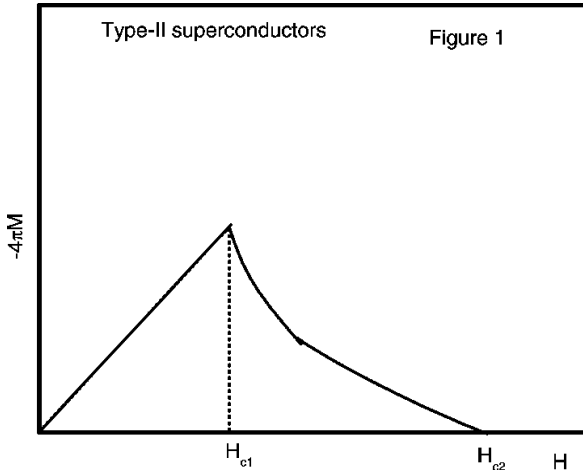


Figure 1. The magnetization *versus* field curve for a type-II superconductor having two critical fields H_{c1} and H_{c2} . In between these two critical fields, the system goes into mixed state.

3. Flux-pinning

Let us consider a slab of hard type II material finite in the x -direction and infinite along y and z directions, subjected to a magnetic field along the z -direction and a current density (shielding or transport) along the y -direction (Figure 2). In this situation, the local field profile can be obtained from the solution of Maxwell's equation $\nabla \times \mathbf{B} = \mu_0 \mathbf{J}$ under appropriate boundary conditions. The one dimensional equation in the above specified geometry is written as :

$$\frac{d}{dx} B_z(x) = \mu_0 J_y(x). \quad (3)$$

Assuming the vortices in a statical equilibrium, the above equation can be viewed as :

$$\Phi_0 \frac{d}{dx} n(x) = \mu_0 J_y(x), \quad (4)$$

where $n(x)$ is the number of vortices per unit area. It is evident from the above equation that there is a gradient of the vortex density perpendicular to the current flow. Under this situation, there are two kinds of forces acting

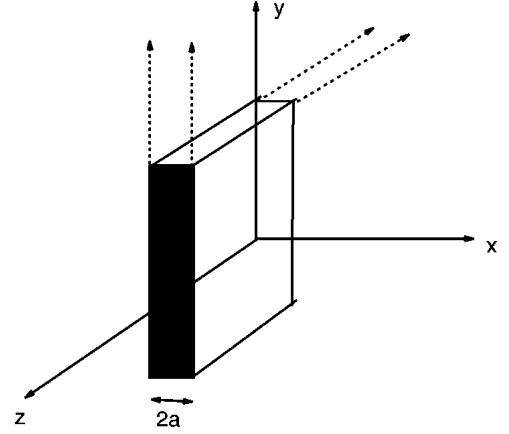


Figure 2. The applied field orientation for $N = 0$ geometry for a slab of infinite extent along y and z directions but of finite thickness ($2a$) along x axis.

on the FLL, *viz.* the inter-vortex interaction resulting from the Lorentz force and the pinning force due to defects. A **critical state** is achieved when the pinning force density F_p is balanced by the Lorentz force density, $F_p = \mathbf{J} \times \mathbf{B}$. (5)

In the present one dimensional case, the previous relation becomes :

$$F_{px} = J_y(x) B_z(x) = \frac{1}{\mu_0} \frac{dB_z}{dx} B_z = \frac{1}{2\mu_0} \frac{d(B_z)^2}{dx}. \quad (6)$$

Hence, eq. (6) implies that a distinct gradient of the vortex line density is sustained by the pinning force in the **critical state**. It also determines the critical current in a superconductor and the critical temperature gradient. Flux pinning prevents the magnetic properties of the superconductors to attain a thermodynamic equilibrium and hence causes irreversibility in its magnetic behaviour. Flux-pinning and the features of critical state are very important from the technical application point of view where large currents and magnetic fields are involved. The origin of the pinning forces against the onset of flux motion arise from the local depressions in the Gibb's free energy of the vortex line. Such depressions can originate through the presence of inhomogeneities in the material in the form of lattice defects, normal inclusions etc. Mere presence of localized pinning sites is not sufficient for obtaining finite pinning forces. Elastic distortions of the flux-line lattice (FLL) are also necessary

to get a non-zero pinning force. For a completely rigid FLL, the net pinning force is zero [3].

From eqs. (4) and (6), it is evident that for any hard type-II superconductor, defining a locally averaged pinning force, one can extract the macroscopic pinning dependent properties like magnetization *etc.* in terms of the critical current density J_c of the superconductor without getting involved into microscopic details of pinning centers. Depending on this basic idea of critical state, Critical State Model description of hard type II materials was developed. In the next section, we shall briefly describe that.

4. Critical state models

In the **critical state**, due to flux-pinning, the superconductor carries the maximum current density everywhere without the appearance of flux-motion. For the analysis of various obtained experimental features in hard type-II superconductors, like irreversibility in magnetization, detailed behaviour of magnetization curves *etc.*, an wide variety of Critical State Models were proposed. These models provide a macroscopic explanation to many experimental features without considering microscopic details like flux-pinning, surface barrier during the entry or exit of flux-lines *etc.* The initial concept of CSM was introduced by Bean in his two works [1,4], where the irreversibility in magnetization behaviour of hard type-II superconductors is explained. These models postulate that for low applied field or currents, the outer part of the sample is in a so-called ‘Critical State’ with special values of the current density and magnetic field such that the interior is shielded from fields and currents. Different models assume different relations between the local field and the current density. It is quite obvious that ‘Critical State’ can be achieved under the application of field as well as transport current. In this Review, we shall discuss about the critical state resulting from the application of the field.

According to the formulation of CSM, the penetration of the fields inside a hard type II material, consists of two steps. First with any change of the external applied field, according to Lenz’s law, surface currents are induced. In the next step, this surface current relaxes into a volume current carrying shell, carrying current equal to the critical current density, enclosing a shielded region. The surface separating the shielded region from the penetrated ones is termed as the *flux-front* and the evolution of the flux-front with gradual change of the applied magnetic field is studied in the CSM formulation. Since with any change in the external field, the modifications in the local field or current always start

from the surface, the irreversibility in the magnetization behaviour is in-built in the CSM description.

In the following subsections, we first describe various classes of problems, which can be solved in the framework of CSM. Next we briefly describe the different propositions of CSM for the initial Bean’s Model. The wide varieties of proposed CSM’s are also mentioned in brief for zero demagnetization factor (N) sample geometry. Starting with initial attempts of solving the CSM for non-zero demagnetization factor samples, we briefly describe the available solutions.

4.1. Classification of solvable problems :

A large variety of different problems which can be solved by using CSM formulations can be widely categorized into the following [5] :

- (I) If the sample dimension along the applied field direction is finite, the demagnetization factor (N) corresponding to the sample geometry is non-zero. For such case, at any general point \mathbf{r} , the direction of local \mathbf{B} is a function of both \mathbf{r} and B_a , the magnitude of the applied field :

$$\mathbf{B} / |\mathbf{B}| = \hat{e}(\mathbf{r}, B_a). \quad (7)$$

This realistic situation is more relevant experimentally. Most of the experimental situations pertain to $N \neq 0$ sample geometry. This class of problem has one more possible complications. As the magnitude of the external field is raised slightly, a new current shell is created in addition to the existing ones. For $N \neq 0$ samples, this current shell produces fields external to itself also and thus modifies the local fields between the final flux front and the sample surface. Whereas, for $N = 0$ geometry, the shielding current carrying shell will modify only the interior field, since the demagnetization factor for the shell itself is zero.

- (II) Well-accepted analytic solutions of all proposed CSM’s are available for the infinite slab or the circular cylinder with the applied field along the infinite dimension. This is $N = 0$ sample geometry. If the sample is of infinite extent along z -direction and the applied field $\mathbf{B}_a = B_a \hat{z}$, for this class of problems, the local field everywhere is either zero or along $\pm \hat{z}$, depending upon the raising, lowering or reversal of the applied magnetic field. Hence for this class :

$$\mathbf{B} / |\mathbf{B}| = \hat{z}. \quad (8)$$

The first CSM proposed by Bean pertains to this particular geometry.

(III) A third class of problem exists for the $N = 0$ sample geometry satisfying eq. (7). This situation can be obtained when a continuously rotating field applied parallel to the plane of an infinite slab. In this case, although the field is applied along the infinite dimension, local field everywhere within the sample obeys eq. (7). It is to be noted that for such class, $|\Delta \times \mathbf{B}| = \mu_0 J_c$, the Maxwell's equation is in general, satisfied with the profile $\mathbf{B}(x)$ not restricted to be lying on a plane. With a given applied field and the boundary condition at the sample surface, the above equation does not have a unique solution. The procedure for choosing one exact solution is discussed in later sections.

4.2. Propositions of CSM :

- (1) Bean's original statement : "Any electromotive force, *however small*, will induce the full current J_c to flow locally. Only three states of current flow are possible with a given axis of the magnetic field : zero current for those regions that have never felt the magnetic field, and full current flow J_c perpendicular to the field axis, the sense of current depending on the sense of the electromotive force accompanying the last local change of the field."
- (2) While considering the ac response of various materials, Clem [6] states that in the CSM, \mathbf{J} is always locally perpendicular to \mathbf{B} . Vectorially, $\mathbf{J}(\mathbf{r}) \cdot \mathbf{B}(\mathbf{r}) = 0$. This is considered to be the second statement of CSM.
- (3) There is another important alternative statement of CSM proposed in Ref. [5] which states that if there is any change in the external applied field, then the distribution of the shielding current $\mathbf{J}(\mathbf{r})$ is such as to minimize the change of the flux contained within the sample with $|\mathbf{J}(\mathbf{r})| \leq J_c$. The inequality on $|\mathbf{J}(\mathbf{r})|$ becomes valid on physical grounds for $N \neq 0$ samples (class I).

4.3. Class I problems :

CSM and its extensions for $N = 0$ sample geometry can explain semi-quantitatively the magnetic irreversibilities observed under quasi-static changes of magnetic field or of temperature. If the smallest dimension of the sample perpendicular to the applied field is D and its dimension along the applied field is L , then these calculations assume that $L/D \rightarrow \infty$. These calculations also predict that the magnetic irreversibility goes linearly to zero with decreasing D . For non-zero irreversibility $D \neq 0$, and the requirement that $L/D \rightarrow \infty$ cannot be satisfied for a sample of finite volume. For realistic samples exhibiting

irreversibility, the calculations must incorporate the fact L/D is finite and the sample is having $N \neq 0$.

The first serious attempt to solve $N \neq 0$ sample started with the early work of Kato [7] and subsequently of Wilson [8]. They have obtained some approximate solutions for cylindrical wire of circular cross section under a transverse field. Kato assumed the flux front to be circular whereas Wilson's solution approximated it to be elliptical. With easy availability of samples in the form of discs and platelets, recent experimental and theoretical studies have mainly focussed on thin samples – discs [9] and strips [10] – in the transverse geometry, with applied field perpendicular to thicker dimension. The case of field-dependent J_c in thin samples has been considered by McDonald and Clem [11], Bhagwat and Chaddah [12] and more recently by Shantsev *et al* [13]. Theoretical study of thin samples affords one simplification. Here, one needs to work only with an 'average' current density, or a current-sheet. The immense complexity associated with the task of determining and studying the movement of the flux-front as the flux penetrates the sample is absent. Bhagwat and Chaddah have also worked with finite samples and have solved a re-statement of CSM for elliptical cylinders in transverse geometry, for a spheroid [14] and also for the general ellipsoid [15]. Navarro and Campbell [16] have followed a numerical procedure for obtaining flux-fronts and magnetization for a sphere, and oblate and prolate spheroids. Prigozhin [17] has worked out a variational formulation and obtained numerical solution for flux-fronts. To determine the hysteresis loss in superconducting wires, Ashkin [18] has worked out the flux-fronts numerically. Telchow and Koo [19] have provided a numerical solution for the flux-fronts and the magnetization curves for a sphere by solving an integral equation. They observe that for samples with cylindrical symmetry, a flux-front can be viewed as a surface of zero vector potential.

More recently, Brandt [20] has extended his earlier solution for thin strips and discs to those having a finite thickness and has worked with a realistic current-voltage law. His solution also involves solving an infinite system of nonlinear differential equations and follows a numerical procedure. However, in his treatment, even the various matrix elements need numerical evaluation.

Thus, for samples with $N \neq 0$, there is no direct analytical formulation of the general problem and a method of solution that yields the evolution of flux-fronts as the external field is applied on a zero field cooled virgin sample of a hard type-II superconductor.

Now, we shall briefly discuss some of the basic differences between the CSM propositions for $N = 0$ and $N \neq 0$ geometry. As described earlier, for a sample with $N = 0$, the local field $\mathbf{B}(\mathbf{r})$ at all points within the sample is along the direction of the applied field. When the externally applied field $\mathbf{H}_a = H_a \hat{z}$ is increased in magnitude, flux front penetrates deeper into the sample and the change in the local field is along \hat{z} everywhere within the sample. The shielding currents set up according to Bean's proposition and the current shell also have $N = 0$. Thus, the local field exterior to the current shell is not modified due to current carried by itself. The situation is not so simple for $N \neq 0$ geometry. First, the flux lines are curved and $\mathbf{B}(\mathbf{r})$ is not along the direction of the applied field. Also the current shell, set up due to the increase of the external field by δH_a , itself has $N \neq 0$ and hence produces field external to itself. Specifically, this causes the change in the local field of the region already carrying shielding current and this last change in $\mathbf{B}(\mathbf{r})$ has different directions at different \mathbf{r} . Shielding currents must now be set up afresh with the sense determined by the second change in $\mathbf{B}(\mathbf{r})$. These fresh currents will again modify the local field everywhere and the whole process will repeat consistently. Hence, rigorous application of Bean's model for $N \neq 0$ samples leads to the result that the magnitude of the shielding current density shall be equal to J_c , while its sense of flow (even during virgin magnetization) is a very complicated function of position. One may also visualize that the average of the shielding current density over a small volume around \mathbf{r} should have the same sense of flow for all \mathbf{r} during virgin magnetization. On the contrary, the magnitude of the locally averaged current density will be less than or equal to J_c . Bean's model, being a macroscopic description, is justified in adapting the alternative view that the shielding current will flow in the same sense at all \mathbf{r} in the current carrying region, but with a magnitude $J_s \leq J_c$. In this paper, an exact solution for a particular $N \neq 0$ geometry is presented.

4.4. Class II problems :

For $N = 0$ sample geometry, eq. (8) is satisfied. There can be various configurations of $B_z(x)$, $J_y(x)$ and $F_p(x)$ that meet the requirement. The Bean model assumes $J_y(x) = J_c = \text{constant}$, while the fixed pinning model assumes $F_p = \text{constant}$, whereas all the other models assume a more complex relationship between the internal field and the current density. For most models, the relationship between $J_y(x)$ and $B_z(x)$ for the slab geometry is generally of the form

$$J_y(B_z) = \frac{J_k}{f(B_z)}, \quad (9)$$

where $f(B_z)$ is a function of the local magnetic field and J_k is a field independent parameter. Eq. (9) is substituted in eq. (4) and the resulting differential equation is solved to obtain the local field profile $B_z(x)$. In the following table, we listed various proposed CSMs [2] and the corresponding references respectively in Tables 1 and 2.

Table 1. Various proposed CSMs and the corresponding J–B relations.

Bean Model	$J(B) = J_c$
Fixed pinning Model	$J(B) = \frac{J_c}{ B(x) /B_k}$
Square root Model	$J(B) = \frac{J_c}{[B(x) /B_k]^{1/2}}$
Kim Model	$J(B) = \frac{J_c}{1 + B(x) /B_k}$
Exponential Model	$J(B) = J_c \exp[- B(x) /B_k]$
Linear Model	$J(B) = J_c - J'_c B(x) /B_k$
Quadratic Model	$J(B) = \frac{J_c}{[1 + B(x) /B_k]^2}$
Triangular pulse Model	$J(B) = J_c(1 - B(x) /B_k)\Theta(B_k - B(x))$
Generalized Model	$J(B) = \frac{J_c}{[1 + B(x) /B_k]^\beta}$

Table 2. The references for the respective CSMs (for more details, reader can consult Ref. [2] and references therein).

Bean Model	Bean 1962, 1964
Fixed pinning Model	Ji <i>et al.</i> , 1989; LeBlanc and LeBlanc, 1992
Square root Model	LeBlanc and LeBlanc, 1992
Kim Model	Kim <i>et al.</i> , 1962, 1963
Exponential Model	Fietz <i>et al.</i> , 1964
Linear Model	Watson, 1968
Quadratic Model	Leta <i>et al.</i> , 1992
Triangular pulse Model	Dersch and Blatter, 1988
Generalized Model	Lam <i>et al.</i> , 1990; Xu <i>et al.</i> , 1990

Among all these models, Bean, Kim and exponential model are mostly used for analysis of the experimental data. For $N \neq 0$ sample geometry, in all the J–B relations, $|B(x)|$ will be replaced by $|\mathbf{B}|$.

4.5. Class III problems :

As mentioned in Refs. [21,5], Bean's original statement of Critical State Model (CSM) does not unambiguously

lead to the final solution when the change in the applied field is in a direction different from that of the initial field. The non-uniqueness of local field profiles is resolved by imposing an additional criterion of minimum flux-change [5]. This criterion enables us to determine uniquely the final metastable state from the various accessible ones. We describe the formulation of the problem by defining a variational functional representing the measure of the change of the flux within the sample.

For getting a unique solution in more general situations, a new criterion of flux-change-minimization was suggested in Ref. [5] and also in subsection 7.1. The statement is based on the physical idea [5] that in response to changes in the external magnetic field, a hard type-II superconductor behaves like a perfect conductor to the extent possible. For a perfect conductor, $\partial \mathbf{B}(\mathbf{r})/\partial t = 0$, and thus $\delta \mathbf{B}(\mathbf{r}) = 0$, for all \mathbf{r} within the sample. Thus, the quantity to be minimized is $\int \delta \mathbf{B}(\mathbf{r}) d\mathbf{r}$. For problems pertaining to case II, the above quantity is a scalar, whereas it is a vector quantity for those of case III. So for the latter class of problems, the quantity to be minimized is $\int |\delta \mathbf{B}(\mathbf{r})|^2 d\mathbf{r}$ [5]. The latter is applicable equally well in both the cases.

In the next sections, we shall briefly discuss about the formulation and results obtained from the solution of some problems of all of these three categories.

5. Class I problems : formulation, solution and applications

In this class, we have chosen an infinite cylindrical sample of any arbitrary cross section and gradually generalized the field directions starting from transverse symmetric [22,23] (along one of the symmetry axis of the transverse cross section) to transverse oblique [24] (along any arbitrary direction in the transverse plane) and finally along any general direction with respect to the cylinder axis [25]. In this Review, we shall discuss the general directional field solution as all the earlier three results can be obtained as a special case of it.

5.1. Analytical formulation for cylinders :

5.1.1. Current density, current shells and flux-fronts :

Let us consider a zero field cooled (ZFC) cylindrical sample subjected to a uniform transverse field. As per the CSM, the sample responds to changes in the external field by setting up an induced current density J_c starting from the surface. The extent of penetration of flux as well as that of induced current density in the sample is limited by the **flux-front**. In other words, during the

virgin curve, in the region interior to the flux-front, both $\mathbf{B} = \mathbf{0}$ and $\mathbf{J} = \mathbf{0}$. In this region, the field generated by induced currents exactly cancels the applied field. The field B_a may be reached by sequentially applying a large number of infinitesimally small steps of δB_a , starting from zero field. At each of these steps δB_a , a new (infinitesimally small) current shell would be set up within the sample generating field in its interior that exactly annuls the change δB_a . An infinitesimal current shell may be viewed as a surface current. Thus, the shielding volume current density can be broken up into an effective succession of surface currents. Since each of these current shells (or the equivalent surface current density) generates uniform interior field, it must have the form given in Refs. [26,25]. The expression for such surface current density on an arbitrary cross sectional cylinder can be derived by utilizing a conformal map, mapping the exterior of the arbitrary cross section to the exterior of a unit circle. For a circular cross section, the surface current density can be exactly calculated.

A given flux-front would be characterized by B_a , the magnitude of the applied field. Thus, flux-fronts form a one-parameter family of surfaces. At zero field, the flux-front coincides with the sample surface. As B_a is increased monotonically, the volume enclosed by the flux-front shrinks in size and more flux penetrates the sample. Eventually at some field B_p , the flux completely penetrates the sample. The magnitude of B_p depends on the critical current density J_c and sample dimensions, and can be deduced from the solution of the model. We shall use the symbol ξ to denote the flux-front parameter. Consequently, the sample surface corresponds to $\xi = 0$, and the innermost flux-front would be identified by $\xi = \xi_a = B_a/\mu_0 J_c b$ [24], where b is the largest transverse dimension of the cross section of the cylinder.

5.1.2. Description of flux-fronts by their conformal map :

For analytical description of the family of flux-fronts, we conceive of a one to one correspondence between members of the family of flux-fronts and a family of conformal mappings characterized by the parameter ξ . We require that the conformal mapping associated with a given flux-front maps it onto a unit circle and its *exterior* onto the *exterior* of the same unit circle. If the cross section of the cylinder be in the complex ζ -plane, the family of conformal mappings can be represented as [23, 24]

$$\zeta = f(u, \xi) = \sum_{n=1}^{\infty} a_n u^{-(2n-3)}, \quad (10)$$

where the coefficients $\{a_n, n = 1, 2, \dots\}$ are in general complex functions of the (real) parameter ξ . In Figure 3,

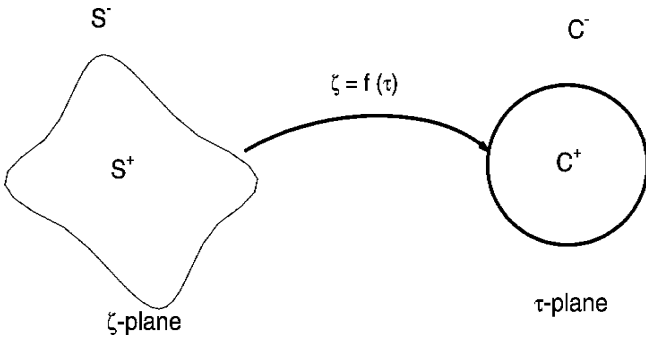


Figure 3. Schematic diagram of the conformal mapping which maps the exterior of an arbitrary cross sectional contour onto the exterior of an unit circle.

we schematically present the conformal map. These will be chosen in the form $a_n = p_n \exp(i\alpha_n)$. Clearly, if we set $u = \exp(i\phi)$, $(-\pi \leq \phi < \pi)$, eq. (10) provides an analytical representation of the flux-front. The initial values of these coefficients viz., $a_1(0), a_2(0), a_3(0), \dots$ etc. are obtained by determining the initial conformal mapping of the exterior of the boundary L of cross section of the cylinder onto the exterior of a unit circle. These coefficients evolve as functions of ξ . The solution consists in obtaining the evolution of the coefficients. The magnetization of the sample is expressible in terms of these coefficients and hence can be obtained.

5.1.3. Surface current density producing uniform interior field :

Let us consider a cylindrical sample placed with its axis along the z -axis (see Figure 4) and let its transverse cross section be bounded by a contour L in the complex ζ -plane. (Although L is a rectangle in Figure 4, the following arguments are valid for any general cross section).

Here $\zeta = x + iy = f(u, \xi)$, with the flux-front parameter ξ , represents the conformal map of the exterior of the contour L to the exterior of the unit circle $u = \exp(i\phi)$ in the complex u -plane [24]. For future convenience, we denote the limit of $f(u, \xi)/u$ as $u \rightarrow \infty$ by the complex number $\Gamma \exp(i\gamma)$. We want to find out the expression for the surface current density, producing a uniform field in a fixed (arbitrary) direction. If the surface current density is represented as $\mathbf{J}_s = \hat{i}J_1^s + \hat{j}J_2^s + \hat{k}J_3^s$, the field produced by it can be written as :

$$\mathbf{B}(\mathbf{r}) = \frac{\mu_0}{4\pi} \int \int_{-\infty}^{+\infty} \frac{\mathbf{J}_s \times (\mathbf{r} - \mathbf{r}')}{|\mathbf{r} - \mathbf{r}'|^3} ds' dz', \tag{11}$$

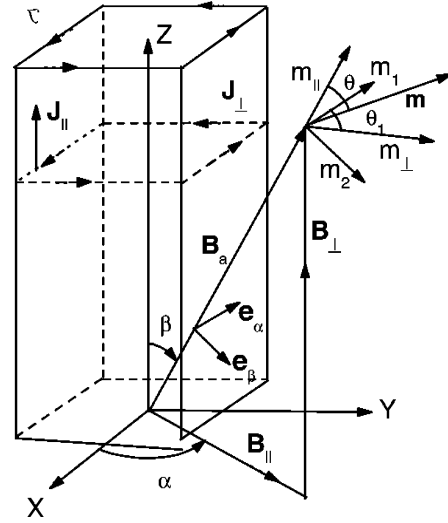


Figure 4. The choice of the coordinate axes and the sample geometry. The sample is assumed to have a rectangular cross section L . The polar coordinates (β, α) are used to specify orientation of the applied field B_a , e_α and e_β are the unit vectors corresponding to α and β . J_\parallel and J_\perp are components of J parallel and perpendicular to the axis of the cylinder. B_\parallel and B_\perp are components of B_a parallel to J_\parallel and J_\perp . m_\parallel and m_\perp are components of magnetization along and perpendicular to the applied field. m_1 and m_2 are the two perpendicular components of magnetization along e_α and e_β .

where ds' is the element of arc on the boundary L such that $ds' dz'$ is the element of surface area on the cylinder. Performing the integration over z' , we get

$$\mathbf{B}(\mathbf{r}) = \frac{\mu_0}{2\pi} \left[\int J_3^s \frac{[-\hat{i}(y-y') + \hat{j}(x-x')]}{(x-x')^2 + (y-y')^2} ds' + \hat{k} \int \frac{J_1^s(y-y') + J_2^s(x-x')}{(x-x')^2 + (y-y')^2} ds' \right]. \tag{12}$$

The two dimensional current density $\hat{i}J_1^s + \hat{j}J_2^s$ must be along the tangent to the curve L . The unit vector \hat{i} along the tangent to the cross sectional contour can be written as $\hat{i} = \hat{i}dx'/ds' + \hat{j}dy'/ds'$. Thus writing $J_1^s = J_\perp^s dx'/ds'$ and $J_2^s = J_\perp^s dy'/ds'$, we may write $\mathbf{J}_s = \mathbf{J}_\perp^s + J_\parallel^s \hat{k}$ with $\mathbf{J}_\perp^s = \hat{i}J_1^s + \hat{j}J_2^s$ and $J_\parallel = J_3^s$. The second term of eq. (12) can be represented as : $\Im \oint [J_\perp^s / (\zeta - \zeta')] d\zeta'$ with ζ as defined earlier and $\zeta' = x' + iy'$. It is clear that the surface current densities $J_3^s \hat{k}$ and \mathbf{J}_\perp^s should produce uniform interior fields respectively transverse and parallel to \hat{k} .

Now, for a cylindrical conductor, the surface current density along the z -axis producing uniform transverse interior field B_\perp inclined at an angle α with the x -axis, can be obtained by solving a boundary value problem

named as Riemann-Hilbert (R-H) problem. We here briefly present the method for solving this R-H problem [27]. In the two dimensional ζ -plane, the region interior and exterior to the contour is denoted as S^+ and S^- . When ζ approaches a point t on L , the limiting values of the complex function $B(\zeta)$, as represented by the Cauchy integral in Ref. [26], is denoted by $B^+(t)$ and $B^-(t)$ depending on whether $\zeta \rightarrow t$ from S^+ or from S^- . If the interior field is along any general direction, we can write :

$$B^+(t) = B_0 = B_1 + \iota B_2, \quad (13)$$

where B_0 is applied field with components B_1 and B_2 along x and y axis, respectively. Using Plemelj formulae [27], one can write :

$$B^+(t) - B^-(t) = \phi(t) = -\iota \mu_0 J_{\parallel}^s \exp(-\iota \omega), \quad (14)$$

where $\tan \omega = dy'/dx'$ and $d\zeta' = dx' + \iota dy'$. Substituting the value of $B^+(t)$ from eq. (13) in the above equation and after slight rearrangement, one gets :

$$\mu_0 J_{\parallel}^s = \iota (B_1 + \iota B_2 - B^-(t)) \exp(\iota \omega).$$

Using the fact that the physically relevant current densities must be real, we can write :

$$\text{Re} \left[(B_1 - B^-(t)) \exp(\iota \omega) \right] = B_2 \sin \omega$$

which can be formulated as a Riemann-Hilbert problem as :

$$\text{Re} (B^-(t) \exp(\iota \omega)) = B_1 \cos \omega - B_2 \sin \omega. \quad (15)$$

Carrying out the transformation from ζ plane $\rightarrow \tau$ plane, such that exterior of L maps onto the exterior of a unit circle, one can write on the circular contour :

$$\begin{aligned} \tilde{B}^-(u) \exp(\iota \tilde{\omega}) + \tilde{B}^+ \exp(-\iota \tilde{\omega}) \\ = 2B_1 \cos \tilde{\omega}(u) - 2B_2 \sin \tilde{\omega}(u). \end{aligned}$$

After some rearrangement, the above equation can be written in the form of homogeneous Hilbert problem as discussed in details in [26] :

$$\tilde{X}^+(u) = G(u) \tilde{X}^-(u),$$

where $\tilde{X}^+(u) = \tilde{B}^+(u) - \bar{B}_0$, $\tilde{X}^-(u) = \tilde{B}^-(u) - B_0$ and $G(u) = -\exp(2\iota \tilde{\omega})$. The general solution of the above equation can be written as :

$$\tilde{X}^-(\tau) = \frac{c_0 + c_1 \tau + \bar{c}_0 \tau^2}{\tau^2 f'(\tau)}.$$

Hence, using the definition of $\tilde{X}^-(\tau)$, we get :

$$\tilde{B}^-(\tau) - \tilde{B}^+(\tau) = \frac{c_0 + c_1 \tau + \bar{c}_0 \tau^2}{\tau^2 f'(\tau)}. \quad (16)$$

Using the boundary condition that as $\tau \rightarrow \infty$, $\tilde{B}^- \rightarrow 0$, the value of the coefficients can be fixed to be $c_0 = \bar{B}_0 \Gamma \exp(\iota \gamma)$ and $\bar{c}_0 = -B_0 \Gamma \exp(\iota \gamma)$. Using eqs. (14) and (16), one can get the expression for current density as :

$$\begin{aligned} \mu_0 J_{\parallel}^s = & -\frac{2B_1 \Gamma \exp(\iota \gamma) \cos \phi}{|f'(\phi)|} \\ & + \frac{2B_2 \Gamma \exp(\iota \gamma) \sin \phi}{|f'(\phi)|} + \frac{c_1}{|f'(\phi)|}. \end{aligned} \quad (17)$$

Resolving the field into its x and y components, viz. $B_{0x} = B_2 = B_0 \cos \alpha$ and $B_{0y} = B_1 = B_0 \sin \alpha$, and incorporating the complex value of γ , the final current density expression can be written as :

$$\mu_0 J_{\parallel}^s = 2\Gamma B_{\perp} \sin(\gamma + \phi - \alpha) / |f'(\phi)|. \quad (18)$$

Here ϕ is the angle between the direction of the field B_{\perp} and the vector representing the location of the current density in the u -plane. The quantity $|f'(\phi)|$ is to be understood as the modulus of the derivative of $\zeta = f(u, \xi)$ with respect to u evaluated at $u = \exp(\iota \phi)$.

Next, the surface current density J_{\perp} producing parallel field B_{\parallel} is simply given by [27]

$$\mu_0 J_{\parallel}^s = B_{\parallel}. \quad (19)$$

In the next section, we shall find out how a given volume current density can be viewed as a succession of surface currents and use it to formulate the CSM for cylindrical samples.

5.1.4. Volume current density :

The volume current density \mathbf{J}_v generates a local magnetic field, which can be expressed as :

$$\mathbf{B}(\mathbf{r}) = \frac{\mu_0}{4\pi} \iiint_{-\infty}^{+\infty} \frac{\mathbf{J}_v \times (\mathbf{r} - \mathbf{r}')}{|\mathbf{r} - \mathbf{r}'|^3} dx' dy' dz'. \quad (20)$$

Performing the z' -integration between the limits $(-\infty, +\infty)$ and changing the variables of integration from (x', y') to (ξ', ϕ') by means of the transformation $\zeta' \equiv x' + \iota y' = f(u', \xi')$, with $u' = e^{i\phi'}$, eq. (5) is transformed to :

$$\mathbf{B}(\mathbf{r}) = \frac{\mu_0}{2\pi} \int \left[J_{\parallel}^v \frac{[-\hat{i}(y-y') + \hat{j}(x-x')]}{(x-x')^2 + (y-y')^2} \right]$$

$$+\hat{k} \left[\frac{J_1^v(y-y') + J_2^v(x-x')}{(x-x')^2 + (y-y')^2} \right] \chi d\xi' d\phi', \quad (21)$$

where $\chi = y_\xi x_\phi - x_\xi y_\phi$, is the Jacobian of the above transformation. Referring to the complex quantities ζ and ζ' defined above, we have $d\zeta' = f_u du = u f'(\phi') d\phi'$. Thus, $|d\zeta'| = ds' = |f'(\phi')| d\phi'$. Further, comparing eq. (21) with (12), we can relate the corresponding surface and volume current densities as

$$J_{||}^s = \frac{J_{||}^v \chi d\xi}{|f'(\phi')|}, \quad J_{\perp}^s = \frac{J_{\perp}^v \chi d\xi}{|f'(\phi')|}. \quad (22)$$

The infinitesimal increment in the applied field, δB_a can be resolved into two components $\delta B_{||} = \delta B_a \cos \beta$ and $\delta B_{\perp} = \delta B_a \sin \beta$. Hence, a comparison of eq. (22) with eqs. (18) and (19) reveals that the volume current density that will shield the interior from the incremental field δB_a has the expressions

$$\mu_0 J_{||}^v = \frac{2\Gamma \delta B_a \sin \beta \sin(\gamma + \phi - \alpha)}{\chi d\xi},$$

$$\mu_0 J_{\perp}^v = \frac{\delta B_a \cos \beta |f'(\phi')|}{\chi d\xi}. \quad (23)$$

It should be noted in passing that (from equations in (23)) \mathbf{J}_v is in general, not perpendicular to $\mathbf{B}_a = B_a(\hat{i} \cos \alpha \sin \beta + \hat{j} \sin \alpha \sin \beta + \hat{k} \cos \beta)$. This suggests a possibility of flux cutting [28] as an inevitable consequence for the general situation. As per the CSM, $|\mathbf{J}_v| = J_c$, the critical current density. We choose the flux-front parameter such that the dimension transverse to the field scales linearly with ξ . Without loss of generality, we assume that the sample surface corresponds to $\xi = 1$, and identify the innermost flux contour by $\xi = \xi_a$ to correspond to the applied field B_a . Thus, the transverse dimension $t(\xi)$ of the flux contour corresponding to ξ is given as $t(\xi) = t(1)\xi$. Now, using eqs. (23) and the CSM condition on the magnitude of the total volume current density viz. $|\mathbf{J}_v|^2 = J_{||}^v{}^2 + J_{\perp}^v{}^2 = J_c^2$, we get the following equation for χ :

$$\mu_0 J_c \chi = \frac{\delta B_a}{\delta \xi}$$

$$\times \sqrt{4\Gamma^2 \sin^2(\gamma + \phi - \alpha) \sin^2 \beta + |f'(\phi)|^2 \cos^2 \beta}. \quad (24)$$

Eq. (24) is valid for all ϕ . Let $\phi_0(\xi)$ be the value of ϕ where the transverse direction intersects the flux contour corresponding to ξ . Substituting $\phi = \phi_0$ in eq. (24) and

denoting the corresponding value of χ by χ_0 , we can express $\delta B_a / \delta \xi$ in terms of χ_0 .

$$\frac{\delta B_a}{\delta \xi} = \frac{\mu_0 J_c \chi_0}{\sqrt{4\Gamma^2 \sin^2(\gamma + \phi_0 - \alpha) \sin^2 \beta + |f'(\phi_0)|^2 \cos^2 \beta}}. \quad (25)$$

Using the above expression for $\delta B_a / \delta \xi$, eq. (25) can be written as

$$\chi = \chi_0 \frac{\sqrt{4\Gamma^2 \sin^2(\gamma + \phi - \alpha) \sin^2 \beta + |f'(\phi)|^2 \cos^2 \beta}}{\sqrt{4\Gamma^2 \sin^2(\gamma + \phi_0 - \alpha) \sin^2 \beta + |f'(\phi_0)|^2 \cos^2 \beta}}. \quad (26)$$

Remembering that $\chi = y_\xi x_\phi - x_\xi y_\phi$ is the Jacobian of transformation, eq. (26) can be viewed as a partial differential equation determining the flux contours if we know χ_0 explicitly as a function of ξ . Direct treatment of such equations is not available in literature. It is possible to convert it into a more familiar matrix equation as will be discussed in the next section.

5.1.5. Determination of flux-contours : matrix equations :

The points on the family of flux contours, when analytically described by a family of conformal mapping characterized by the parameter ξ , are given by

$$x + iy = \sum_{n=1}^{\infty} p_n(\xi) \exp(i\Omega_n),$$

for $-\pi < \phi \leq \pi$, with $\Omega_n = \gamma_n - (2n - 3)\phi$. As mentioned earlier the parameter ξ is defined in terms of the scaling of the transverse dimension $t(\xi)$ of the flux contour. A line through the origin that lies in the $x - y$ plane and is perpendicular to the field direction is given by the equation $x \cos \alpha + y \sin \alpha = 0$. The point of intersection of the line with the flux contour corresponds to the angle $\phi_0(\xi)$. The equation that determines ϕ_0 can be expressed as

$$\sum_{n=1}^{\infty} p_n \cos(\Omega_n^0 - \alpha) = 0, \quad (27)$$

where $\Omega_n^0 = \gamma_n - (2n - 3)\phi_0$. Using the above equation we can write the transverse dimension of the ξ -flux contour as

$$t(\xi) = \sum_{n=1}^{\infty} p_n \sin(\Omega_n^0 - \alpha) = t(1)\xi. \quad (28)$$

Eq. (28) defines the parameter ξ . The quantity χ can be expressed in the form $2i\chi = f_\xi \overline{f_\phi} - \overline{f_\xi} f_\phi$. Performing an explicit calculation we get

$$\chi = \sum_{m,n=1}^{\infty} (2m-3)p_m \times [p'_n \cos(\Omega_m - \Omega_n) + p_n \overline{\gamma}'_n \sin(\Omega_m - \Omega_n)]. \quad (29)$$

Using eqs. (27-29), we can evaluate the expression for χ_0 that does not involve the derivatives of p_n and γ_n .

$$\chi_0 = t(1) \sum_{n=1}^{\infty} (2n-3)p_n \sin(\Omega_n - \alpha), \quad (30)$$

where the transverse dimension of the sample, $t(1) = \min(a/\sin \alpha, b/\cos \alpha)$. It is to be noted that χ_0 is a function of ξ alone. Thus, the right hand side of eq. (26) is known in terms of the values of p_n and γ_n and does not involve their derivatives. The expression (29) for χ can be transformed to the following form

$$\chi(\xi, \phi) = \sum_{k=0}^{\infty} U_k \cos 2k\phi + V_k \sin 2k\phi, \quad (31)$$

where

$$U_k = \sum_{m=1}^{\infty} (2m+2k-3)p_{m+k} \{p_m \gamma'_n \sin(\gamma_m - \gamma_{m+k}) - p'_m \cos(\gamma_m - \gamma_{m+k})\} + \sum_{m=k+1}^{\infty} (2m-2k-3)p_{m-k} \{p_m \gamma'_n \sin(\gamma_m - \gamma_{m-k}) - p'_m \cos(\gamma_m - \gamma_{m-k})\}, \quad (32)$$

$$V_k = \sum_{m=1}^{\infty} (2m+2k-3)p_{m+k} \{p_m \gamma'_n \cos(\gamma_m - \gamma_{m+k}) - p'_m \sin(\gamma_m - \gamma_{m+k})\} - \sum_{m=k+1}^{\infty} (2m-2k-3)p_{m-k} \{p_m \gamma'_n \cos(\gamma_m - \gamma_{m-k}) - p'_m \sin(\gamma_m - \gamma_{m-k})\}. \quad (33)$$

Let the Fourier cosine and sine coefficients of the right hand side of eq. (26) be denoted by c_k and d_k respectively. Eq. (26) implies $U_k = c_k$ and $V_k = d_k$. This leads to two matrix equations

$$Ap' + Bq = c, \quad Cp' + Dq = d. \quad (34)$$

Here p, q are column vectors with elements p_n and

$q_n = p_n \alpha'_n$, respectively and the elements of matrices A, B, C and D are function of p_n and γ_n and can be obtained as

$$A_{km} = -(2m+2k-3)p_{m+k} \cos(\gamma_m - \gamma_{m+k}) - (2m-2k-3)p_{m-k} \cos(\gamma_m - \gamma_{m-k}) \Theta_{m-k}, \quad (35)$$

$$B_{km} = (2m+2k-3)p_{m+k} \sin(\gamma_m - \gamma_{m+k}) + (2m-2k-3)p_{m-k} \sin(\gamma_m - \gamma_{m-k}) \Theta_{m-k}, \quad (36)$$

$$C_{km} = (2m+2k-3)p_{m+k} \sin(\gamma_m - \gamma_{m+k}) - (2m-2k-3)p_{m-k} \sin(\gamma_m - \gamma_{m-k}) \Theta_{m-k}, \quad (37)$$

$$D_{km} = (2m+2k-3)p_{m+k} \cos(\gamma_m - \gamma_{m+k}) - (2m-2k-3)p_{m-k} \cos(\gamma_m - \gamma_{m-k}) \Theta_{m-k}, \quad (38)$$

where the symbol $\Theta_{m-k} = 0$ for $m \leq k$, and $= 1$ otherwise. The matrix eqs. (34) are solved numerically by truncating the matrices as followed in Refs. [24,25].

5.1.6. Numerical scheme :

To solve the coupled equations given in (34) numerically, we first eliminate p'_n from the second equation and solve for q . Using the value of q , p'_n is determined from the first of eq. (34). Having obtained the quantities p'_n and $q_n = p_n \gamma'_n$, we can find $p_n(\xi + \Delta\xi)$ and $\gamma_n(\xi + \Delta\xi)$.

$$p_n(\xi + \Delta\xi) = p_n(\xi) + \Delta\xi p'_n(\xi), \quad (39)$$

$$\gamma_n(\xi + \Delta\xi) = \gamma_n(\xi) + \Delta\xi \gamma'_n(\xi). \quad (40)$$

The initial values $p_n(1)$ and $\gamma_n(1)$ are known from the equation of the sample surface. Eqs. (39) and (40) successively determine $p_n(\xi)$ and $\gamma_n(\xi)$. For calculation of magnetization also we have to preserve the values of these coefficients and also of χ_0 at each step of size $\Delta\xi$. For our numerical calculations, we have used a step size $\Delta\xi_n = 0.002$.

We have worked out our results for a special case of a cylinder of rectangular cross section. The rectangle has longitudinal and transverse dimensions $2a$ and $2b$, respectively with $a = 0.6$ and $b = 1.0$. To determine the initial values, $p_n(1)$ and $\gamma_n(1)$ we begin with the conformal mapping that maps the exterior of the rectangular cross sectional contour to the exterior of an unit circle. The most general such transformation from (the rectangle in) the ξ -plane to the circle (in the u -plane) can be written as given in Ref. [29]

$$\zeta = c e^{i\gamma} \int_{u_0}^u \frac{\{(t^2-1)(t^2-k^2)\}^{1/2}}{t^2} dt + \delta. \quad (41)$$

Here c , k , γ and δ are constants, and $u(|u| > 1)$ and $u_0(|u_0| > 1)$ are two points exterior to the unit circle. In our case, we have chosen the phase factor γ in such a way that the sides of the rectangle are parallel to the coordinate axes. The right hand side of eq. (22) can be expanded in powers of $(1/u)$; the coefficients in the expansion provide the required initial values of p_n and γ_n . The sides of the rectangle are expressed in terms of elliptic functions.

5.2. Magnetization curves :

The magnetization for a ZFC infinite cylindrical sample can be obtained from the expression :

$$\mathbf{m}_v = \frac{1}{2A} \iint r' \times \mathbf{J} dx' dy'. \quad (42)$$

Here, A is the area of transverse cross section of the cylinder, which for rectangular cross section is $4ab$, with sides $2a$ and $2b$. As seen before, the total current \mathbf{J} can be written as

$$\mathbf{J} = J_{\perp}^v \frac{dx}{ds} \hat{i} + J_{\perp}^v \frac{dy}{ds} \hat{j} + J_{\parallel}^v \hat{k}. \quad (43)$$

From eqs. (42) and (43), changing the variables of integration from (x', y') to (ξ', ϕ') and using the corresponding volume current density expressions, the different components of m_v can be written as follows.

$$\begin{aligned} \mu_0 m_{vx} = & \frac{\pi \sin \beta}{A} \int_0^{\xi_a} p_1 \{ p_1 \cos \alpha \\ & - p_2 \cos(\alpha_2 + \alpha_1 - \alpha) \} \left[\frac{\delta B_a}{\delta \xi} \right]_{\xi=\xi'} d\xi', \end{aligned} \quad (44)$$

$$\begin{aligned} \mu_0 m_{vy} = & \frac{\pi \sin \beta}{A} \int_0^{\xi_a} p_1 \{ p_1 \sin \alpha \\ & - p_2 \sin(\alpha_2 + \alpha_1 - \alpha) \} \left[\frac{\delta B_a}{\delta \xi} \right]_{\xi=\xi'} d\xi', \end{aligned} \quad (45)$$

$$\begin{aligned} \mu_0 m_{vz} = & \frac{\pi \cos \beta}{2A} \sum_{m=1}^{\infty} \int_0^{\xi_a} (2m-3) p_m^2 \\ & \times \left[\frac{\delta B_a}{\delta \xi} \right]_{\xi=\xi'} d\xi'. \end{aligned} \quad (46)$$

The quantity $\delta B_a / \delta \xi$ is given by eq. (25). The applied

field B_a corresponding to the parameter value ξ_a is obtained from the same equation.

$$\frac{B_a}{B^*} = - \int_{\xi_a}^1 \frac{\chi_0 d\xi}{b \sqrt{4\Gamma^2 \sin^2(\gamma + \phi_0 - \alpha) \sin^2 \beta + |f'(\phi_0)|^2 \cos^2 \beta}}, \quad (47)$$

where $B^* = \mu_0 J_c b$. Full flux penetration corresponds to $\xi_a = 0$ when the innermost flux front reduces to a point or line. The corresponding field B_p is obtained from eq. (34) with lower limit zero.

Knowing the cartesian components of virgin magnetization, we can calculate the parallel and two perpendicular components. The required expressions are

$$m_{\parallel} = (m_{vx} \cos \alpha + m_{vy} \sin \alpha) \sin \beta + m_{vz} \cos \beta, \quad (48)$$

$$m_{\perp}^1 = m_{vx} \sin \alpha - m_{vy} \cos \alpha, \quad (49)$$

$$m_{\perp}^2 = -(m_{vx} \cos \alpha + m_{vy} \sin \alpha) \cos \beta + m_{vz} \sin \beta. \quad (50)$$

The hysteresis loops for the above components can be obtained as usual (as described in Refs. [24,25]). In the next subsection, we shall briefly describe some results of our calculations and their realistic applications.

5.3. Results and discussion :

We divide this subsection into two. In the first one, we shall describe some important details of the flux-penetration characteristics when the applied field is along any arbitrary direction in the transverse plane (transverse oblique). In the next part, some applications of the general field directions are also described.

5.3.1. Transverse oblique field direction :

For illustration purpose, we choose elliptical cylinders. We have presented in Figure 5, the flux-contours for three different angles of orientation (α) of the applied field for the sample ($a = 0.4$, $b = 1.0$). It is seen in Figure 5, that the flux-contours all have a notch (apex). The apex leaves the sample surface as the applied field is increased. The result that apex of the flux contour leaves the sample surface is in general agreement with other numerical calculations for the case $\alpha = 0^\circ$ and this feature has also been justified on physical grounds [23, 30]. Apex represents the point on a flux-contour where \mathbf{J} vanishes. Figure 6 depicts the movement of the apex for different α values. The movement, in general, is along a path curved near the sample surface and is almost linear otherwise. As the field penetrates the sample, the curve generated by the movement of the apex divides the

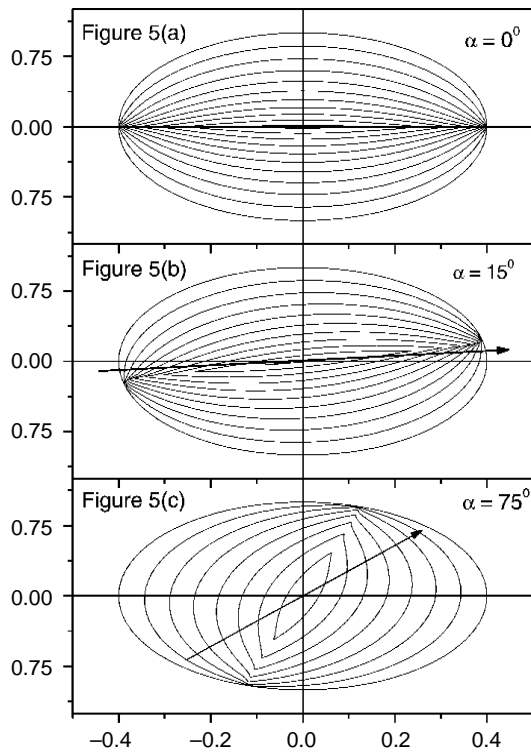


Figure 5. Flux-contours for an elliptical cylindrical sample with the semi-axes $a = 0.4$ and $b = 1.0$. The outermost curve corresponds to the sample surface ($B_a = 0$). Successive contours correspond to a change $\delta B_a = 0.042H^*$. Results are shown for three orientations of the applied magnetic field (a) $\alpha = 0^\circ$, (b) $\alpha = 15^\circ$, (c) $\alpha = 75^\circ$ measured from the x -axis. The arrowheaded line in the figures shows the direction of the applied field.

current carrying region into ones carrying the current density $+J_c$ and $-J_c$. In the case of an elliptical cylinder for $\alpha = 0^\circ$ and 90° and for a circular cylinder for all α values, the apex moves along a straight line parallel to the field direction. The linear portion of the curve is, in general, not parallel to the applied field. The angle between the two, however, progressively decreases as the field orientation approaches 90° .

At first sight, the result presented in Figure 6 appears contradictory to what one would expect from asymptotic considerations. At very high applied fields (beyond the field for full penetration), the whole of sample carries shielding currents and an increase in the external field does not lead to setting up of additional currents. At this stage, one would imagine that the change δB in the local field is equal to the change δB_a in the applied field. Thus, if B_a is increased at a constant rate, it gives rise to an electric field E that vanishes along the direction of δB_a . Since current must flow in the direction of E , $E = \mathbf{0}$ line must also represent the line of separation between the current densities $\pm J_c$. It is to be noted, however, that before full penetration, it is not the electric

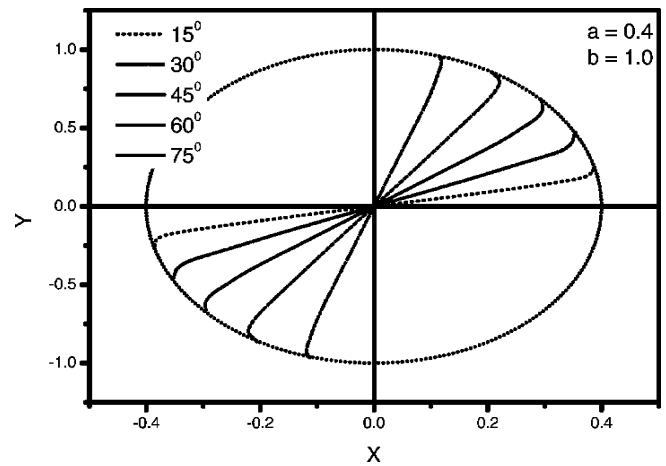


Figure 6. Movement of the “apex” of various flux fronts for different orientations of the applied field. For the field direction α the apex follows a curved path, the linear portion of which has a slope different from α .

field accompanying δB_a alone, that governs apex movement. One must also consider a contribution coming from the δB_J generated by the induced currents. A straightforward but detailed calculation reveals that the local electric field due to δB_J (generated by the current density) contains a term that exactly cancels that coming from the change δB_a . The resulting E leads to the apex movement depicted in Figure 6. All along the process of field penetration, δB_a is assumed to change *quasi-statically*. Thus beyond full penetration, an increase δB_a would generate a surface current density to shield the interior from the change. The surface current density would relax into a current shell (volume current density), the net current density would now exceed the critical current density J_c . The relaxation would then continue by transferring the excess current on the next current shell and the process would continue until the excess current is transferred on to the innermost current shell. Once the change δB_a has been established all over the sample, J in the innermost shell that is in excess of J_c would start decaying. The direction of E in the shells external to the innermost shell does not change during the decay of J leaving the current distribution there unchanged. By a detailed calculation of the local electric field [24], it is straightforward to show that the direction of current density is decided by that of the local E .

The extent of proximity of the slope of the linear portion of the apex movement curve and that of the applied field direction depends on the inherent sample asymmetry about the applied field direction. The more asymmetric the sample, the more is the deviation of the above mentioned slope from the applied field direction.

In Figure 7(a), the virgin magnetization curves for different angles of field orientation are plotted. The values of saturation magnetization (M_{sat}) and field for full penetration (B_p) vary between the maximum for $\alpha = 0^\circ$ and minimum for 90° . At each stage of field penetration, we have checked that the field generated by the induced current distribution, everywhere within the flux-contour, indeed cancels the applied field. The direction of the magnetization is, however, different from that of the applied field, implying the existence of a perpendicular component to magnetization. In Figure 7(b), we have

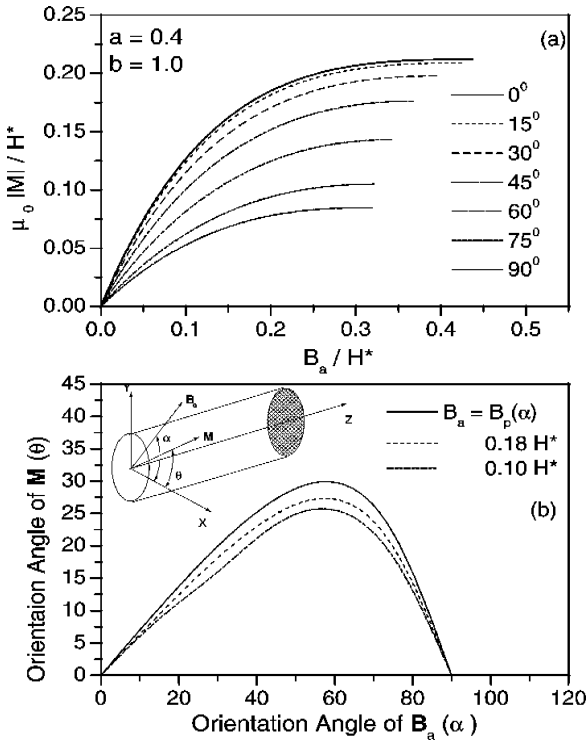


Figure 7. (a) The virgin magnetization curves for different orientations of the applied magnetic field for $B_a \leq B_p$, the field corresponding to full penetration. The elliptical sample has semi-axes $a = 0.4$ and $b = 1$. (b) Orientation angle of M as a function of the orientation angle α of the applied field for different B_a values.

plotted the orientation angle θ of M as a function of the orientation angle α of the applied field B_a for two fixed field values as well as at the saturation field B_p . The geometry of the sample is shown as an inset. This figure compares well with Figure 5 of Ref. [30]. The authors of Ref. [30] have seen the same kind of behaviour for an intrinsically isotropic sample (PbMoS) and also for a sample having intrinsic anisotropy (YBCO). Both of samples are having the same highly geometrically anisotropic shape (thin platelets). We have reproduced the same behaviour only considering the effect of geometric anisotropy. This supports the validity of the theoretical study of effects of only geometric anisotropy.

To estimate the effects on the order of magnitude of some measurable quantities, we considered a model current distribution as $\pm J_c$ on either side of a line through the centre, parallel to the applied field and evaluated expressions for saturation magnetization M_{sat} and the corresponding field B_p . As expected, for $\alpha = 0^\circ$ and 90° , the results obtained from the model current distribution coincide with exact results (obtained by our numerical procedure). For intermediate values of α , the model current distribution leads to results close to the exact results. It is clear, however, that the true values of M_{sat} and B_p depend on the detailed description of field-penetration. Further, as per the model calculation, the directions of both B_p and M_{sat} are not along the applied field direction. We have shown the angle dependence of B_p , M_{sat} , B_p and M_{sat} in Figure 8. The mismatch between the model and the exact values of these quantities is apparent. The true separation between the regions carrying $\pm J_c$ at full penetration is depicted in Figure 6.

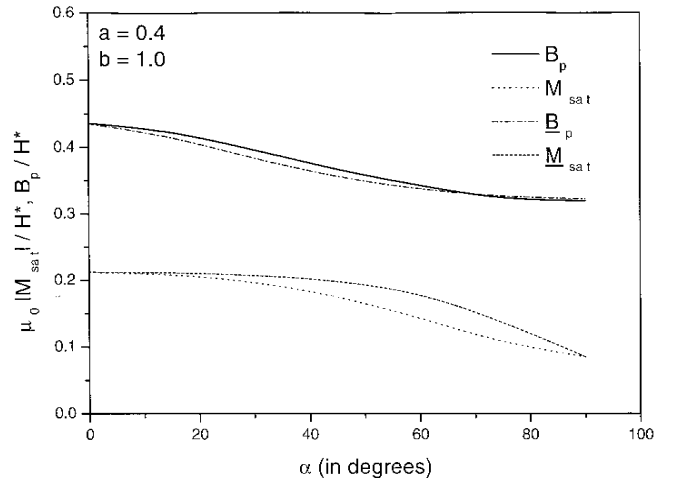


Figure 8. The variation of saturation magnetization M_{sat} and the field for full penetration B_p , as a function of α . We have also plotted the quantities B_p and M_{sat} as a function of α for a model current distribution.

We now present some results to show that our method of solution can be utilized to estimate the effects of geometric anisotropy [31]. As seen earlier, for a totally isotropic shape like a circular cylinder, the apex movement curve is a straight line parallel to the applied field for all α values. We have studied the variation of the deviations (Δ) of the apex movement curve from the applied field direction at the centre of the sample as a function of different aspect ratios (γ) for three different α values in Figure 9(a). The variation of Δ with γ is maximum for $\alpha = 45^\circ$ and with increase or decrease of α the rate of variation decreases. For asymmetric samples, the perpendicular component of magnetization acquires a non-

zero value and the magnitude of it increases with the increase of the sample asymmetry. In Figure 9(b), we have plotted the variation of the ratio of perpendicular and the parallel components of magnetization (M_{\perp}/M_{\parallel}) as a function of γ for three different α values. For γ less than a certain value (~ 0.4), largest rate of variation is observed for greater α values. In Figure 9(c), the variation

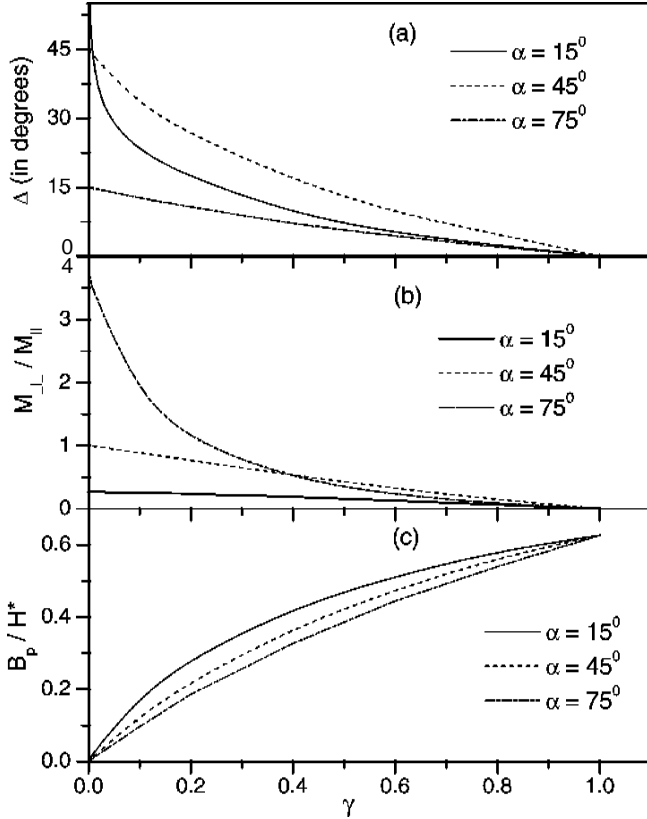


Figure 9. The variation of (a) Δ , (b) M_{\perp}/M_{\parallel} and (c) B_p/B^* as a function of the aspect ratio (γ) for three different angles of orientation (α) of the transverse oblique applied field.

of the field for full penetration (B_p) is depicted as a function of γ for three different α values. For very thin sample as well as for circular cylinder ($\gamma = 1$), any field orientation will lead to the same full penetration field. For intermediate γ , value of B_p is more for less α . In Figure 10, we have studied the variation of (a) Δ , (b) M_{\perp}/M_{\parallel} and (c) B_p/B^* as a function of α for two different γ . The overall rate of change of Δ and M_{\perp}/M_{\parallel} is more for less γ , whereas for B_p/B^* , the situation is reversed.

5.3.2. General field direction :

We have studied the problem of flux penetration for infinite cylinder of arbitrary cross section under general field direction [25]. The results are presented for a special case of an infinite cylinder of rectangular cross section.

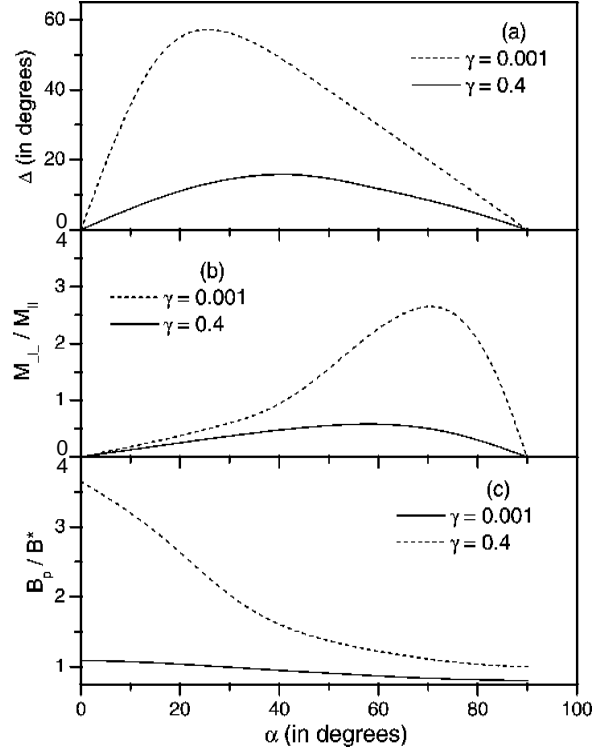


Figure 10. The variation of (a) Δ , (b) M_{\perp}/M_{\parallel} and (c) B_p/B^* as a function of α for two different γ .

The different flux contours in the transverse plane of the cylinder are plotted in Figure 11 for a definite azimuthal orientation ($\alpha = 45^\circ$). Four curves are obtained for four different polar orientations. In a similar way, Figure 12 represents the flux contours for a fixed polar orientation ($\beta = 45^\circ$) and for different azimuthal orientations (α). Returning to Figure 11, when $\beta = 0^\circ$, (Figure 11(a)) the field is along the axis of the cylinder and the flux-contours are independent of α values (in fact, α is not well defined for this case). As is well known, the successive flux contours are then equidistant from each other.

In Figure 13, the hysteresis loops are plotted for (a) m_{\parallel} and components of m_{\perp} , m_{\perp}^1 (b) and m_{\perp}^2 (c) for $\alpha = 45^\circ$ and $\beta = 60^\circ$. Each figure contains a virgin curve, one small loop with reversal field below B_p and another loop with reversal field at B_p and a big loop, with reversal field value beyond B_p . A detailed survey of hysteresis loops for different $\{\alpha, \beta\}$ combinations reveals that the sign of m_{\parallel} and one of the perpendicular component of magnetization is opposite to that of the other perpendicular component.

In Figure 14, the variation of the full penetration field (B_p) and the saturation value of magnetization (m_{sat}) is shown as functions of α and β . From Figures 14(b)

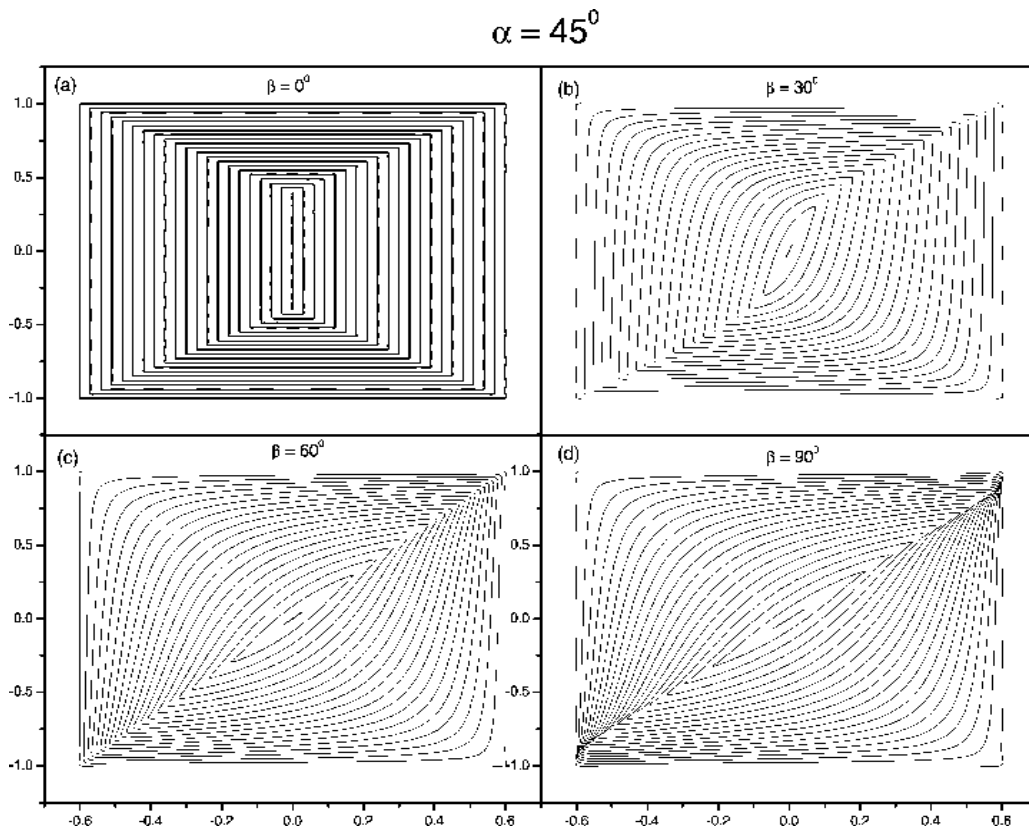


Figure 11. The flux contours for different values of the applied field for a fixed azimuthal orientation $\alpha = 45^\circ$ and for four different polar orientations (a) $\beta = 0^\circ$, (b) $\beta = 30^\circ$, (c) $\beta = 60^\circ$, (d) $\beta = 90^\circ$.

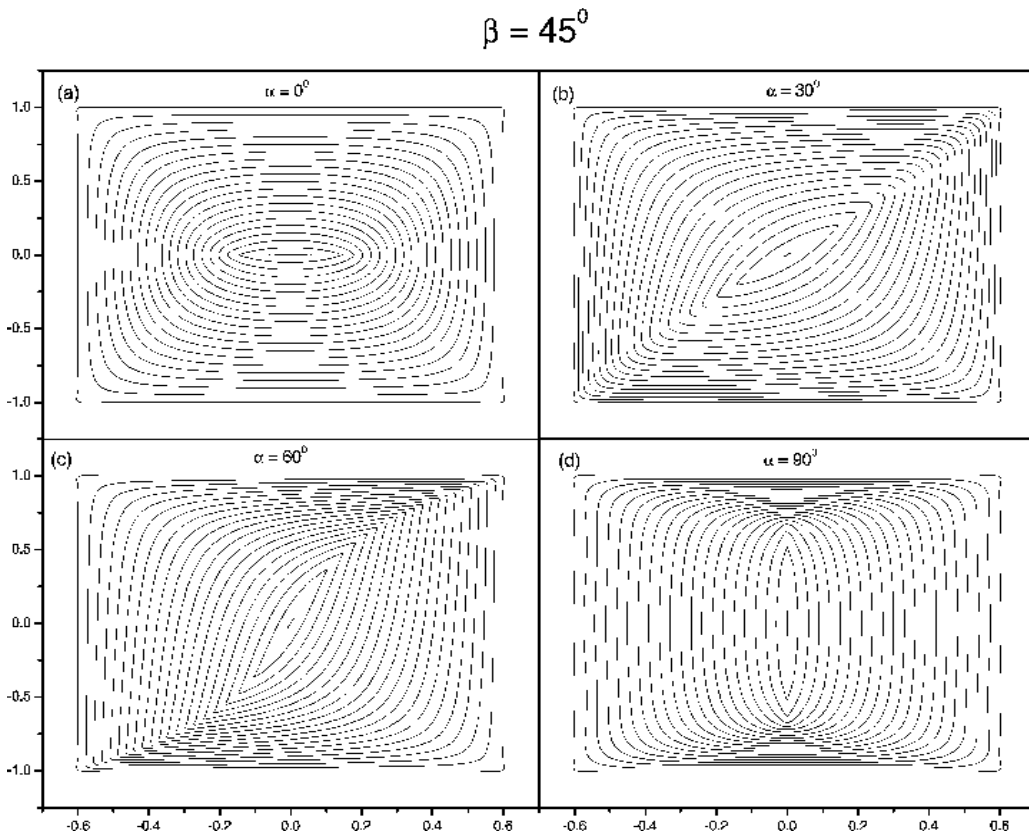


Figure 12. Flux contour configuration for a fixed polar orientation $\beta = 45^\circ$ and for four different azimuthal orientations (a) $\alpha = 0^\circ$, (b) $\alpha = 30^\circ$, (c) $\alpha = 60^\circ$, (d) $\alpha = 90^\circ$.

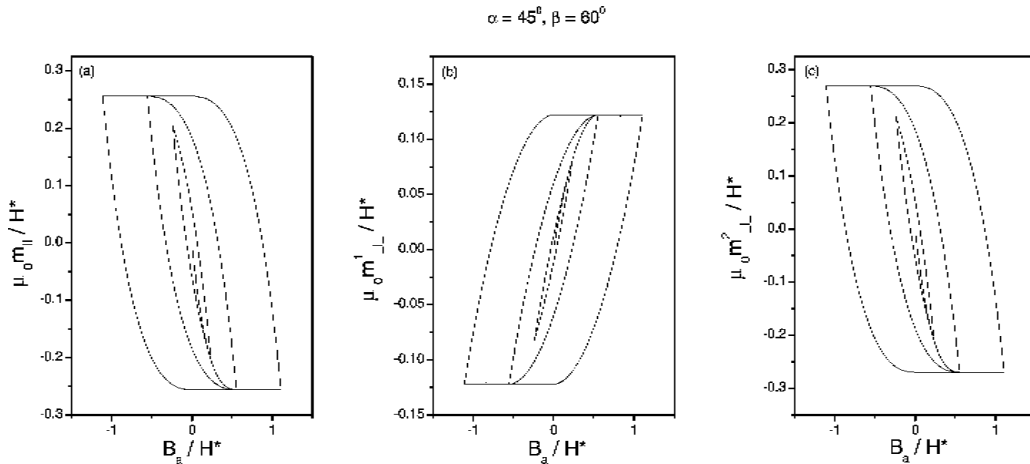


Figure 13. Magnetization hysteresis loops for the m_{\parallel} (a), m_{\perp}^1 (b) and m_{\perp}^2 (c) for $\alpha = 45^\circ$ and $\beta = 60^\circ$. The small loop corresponds to a reversal field of $0.2381H^*$ and the second loop is at full penetration field ($B_p = 0.5539H^*$). For the big loop the reversal field is $2B_p$.

and d), it is observed that different α -curves meet at $\beta = 0^\circ$, the latter corresponds to parallel field geometry (also the dotted line in Figures 14(a) and 14(c)). This

supports the earlier mentioned fact that when $\beta = 0^\circ$, all α values will result in the same flux-contour configuration and hence produce the same B_p and m_{sat} .

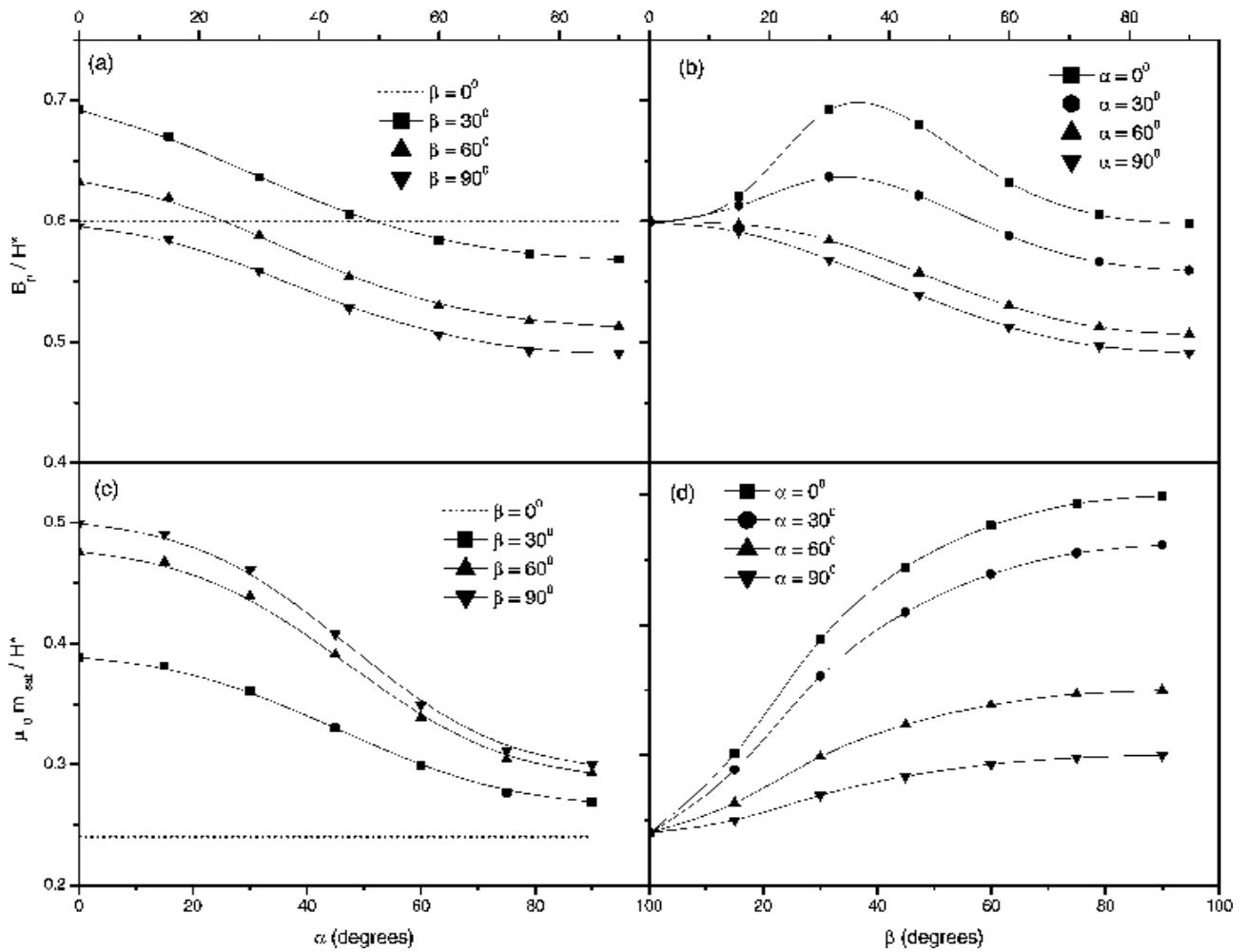


Figure 14. The variations of (a) full penetration value of the field (B_p) with respect to the change in azimuthal orientations α for different polar orientations β , (b) B_p versus β curves for different α values, (c) the saturation magnetization m_{sat} versus α for different β values and (d) m_{sat} versus β for different α values.

We shall now briefly describe two applications of this general formulation of CSM for cylinders. In the first one, we shall utilize this result to calculate the ac susceptibility components (§ 5.3.3) and in the next, reformulate our scheme with stepwise modified J_c (§ 5.3.6) to interpret experimental results.

5.3.3. ac susceptibility calculations :

To investigate the nonlinear dynamic response of hard type-II materials, measurement of the fundamental and higher harmonics of ac susceptibility is a powerful technique [33–35]. Such measurements offer many possibilities to analyse the macroscopic properties of an wide varieties of vortex phases in type-II materials (including thermal instability induced phases in HTSCs) such as : the transition temperature of each structural phase in a multiphase material, investigation of irreversibility line, to measure the critical current density and pinning potential, to separate the inter-grain and intra-grain contribution in a polycrystalline sample, determination of the critical magnetic fields (H_{c1} and H_{c2}) and so on.

Here, we deal with an infinite cylinder of any arbitrary cross section subjected to any general directional ac field $B_a = B_{ac} \cos \omega t$. The fundamental and higher harmonic response of the parallel and two perpendicular components of ac susceptibility are investigated with the variation of ac field amplitude, polar or azimuthal orientation of the applied field. The effect of geometrical anisotropy on the fundamental and higher harmonic ac response of the sample is also studied, by varying the a/b ratio of a rectangular cylinder for various values of the ac field amplitude. The behaviour obtained for higher harmonic generation have close resemblance to the experimental results shown in Refs. [35,36]. In all these cases, we assume the bulk pinning to be the basic mechanism to induce irreversibility (neglecting surface barrier), *i.e.* within the CSM description. For simplicity, the critical current J_c is considered to be independent of the local field (Bean Model). As mentioned in Ref. [37], the ac susceptibilities obtained by following the CSM description are ‘*quasi-static*’, *i.e.* independent of the frequency of the ac field. These only depend on the amplitude of the ac field. Also while calculating the higher harmonics, it is observed, as expected, non-zero values for only odd harmonics. Due to the symmetry of the increasing and decreasing field branches of the hysteresis cycles, even harmonics are zero. Of course, one can get non-zero

even harmonics either by applying a dc bias or by imposing a field dependence over J_c , such that the hysteresis cycle becomes highly asymmetric.

5.3.4. Analytical formulation :

Consider an infinite cylinder of any arbitrary cross section subjected to an ac field $B_a = B_{ac} \cos \omega t$ along any general direction having a polar orientation β and an azimuthal orientation α . The field orientation with respect to the sample is as shown in Figure 3. The magnetic susceptibility tensor under such a general applied field direction is defined by the equation :

$$\begin{pmatrix} \mu_0 m_x \\ \mu_0 m_y \\ \mu_0 m_z \end{pmatrix} = \begin{pmatrix} \chi_{11} & \chi_{12} & \chi_{13} \\ \chi_{21} & \chi_{22} & \chi_{23} \\ \chi_{31} & \chi_{32} & \chi_{33} \end{pmatrix} \begin{pmatrix} B_x \\ B_y \\ B_z \end{pmatrix}. \quad (51)$$

To have a close comparison with the experiments, we can rewrite the above equation in terms of the parallel and two perpendicular components of magnetization as :

$$\begin{pmatrix} \mu_0 m_{\parallel} \\ \mu_0 m_{\perp}^1 \\ \mu_0 m_{\perp}^2 \end{pmatrix} = \begin{pmatrix} \chi_{11} & \chi_{12} & \chi_{13} \\ \chi_{21} & \chi_{22} & \chi_{23} \\ \chi_{31} & \chi_{32} & \chi_{33} \end{pmatrix} \begin{pmatrix} B_x \\ 0 \\ 0 \end{pmatrix}. \quad (52)$$

It is obvious from the above equation that knowledge about the parallel and two perpendicular components of magnetization for a particular orientation of the applied magnetic field leads to the evaluation of the first column of the susceptibility matrix. In a similar way, applying the field along three orthogonal directions, one can evaluate all the elements of the susceptibility matrix. Under the application of an ac field, the elements of the tensor are complex. Hence one can write,

$$\begin{aligned} \chi_{11} = \chi_{\parallel} = \chi'_{\parallel} + i\chi''_{\parallel}, \quad \chi_{21} = \chi_{\perp}^1 = \chi'_{\perp}^1 + i\chi''_{\perp}^1, \\ \chi_{31} = \chi_{\perp}^2 = \chi'_{\perp}^2 + i\chi''_{\perp}^2. \end{aligned} \quad (53)$$

For evaluation of the parallel and perpendicular components of magnetization, we utilized our formulation used in earlier sections. With the help of those expressions, one can numerically evaluate the in-phase dispersion and out-of-phase absorption components of fundamental and higher harmonics of ac susceptibility as :

$$\chi'_i(n) = \frac{\mu_0}{\pi B_{ac}} \int_0^{2\pi} m_i(t) \cos n\omega t d(\omega t), \quad (54)$$

$$\chi_i''(n) = \frac{\mu_0}{\pi B_{ac}} \int_0^{2\pi} m_i(t) \sin n\omega t d(\omega t), \quad (55)$$

where i stands for the parallel or the respective perpendicular components of magnetization and susceptibility and n denotes the order of the higher harmonics, $n = 1$ specifying the fundamental component. With the help of the above two equations, we calculated the fundamental and higher harmonics χ' and χ'' components for the parallel and both of the perpendicular components of ac susceptibility.

5.3.5. Results and discussions

For the purpose of illustration, we consider a rectangular cylinder of a/b ratio 0.6 and plot the real, imaginary as well as the magnitude (modulus) of the fundamental and one odd higher harmonics of the parallel ac susceptibility component as a function of the ac field amplitude and with variable orientations in Figures 15–20. In these figures, we have plotted the susceptibility components with respect to the ac field amplitude normalized by $B^* = \mu_0 J_c b$, where b is longer dimension of the rectangular

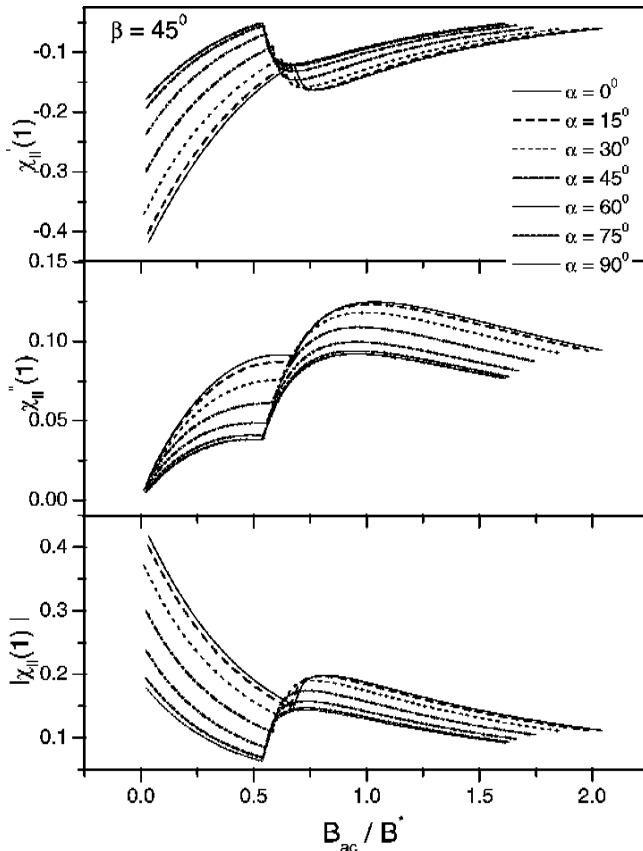


Figure 15. Real (χ'), imaginary (χ'') and modulus ($|\chi|$) of the parallel fundamental ac susceptibility as a function of the normalized ac field amplitude for $\beta = 45^\circ$, α varying from 0° to 90° .

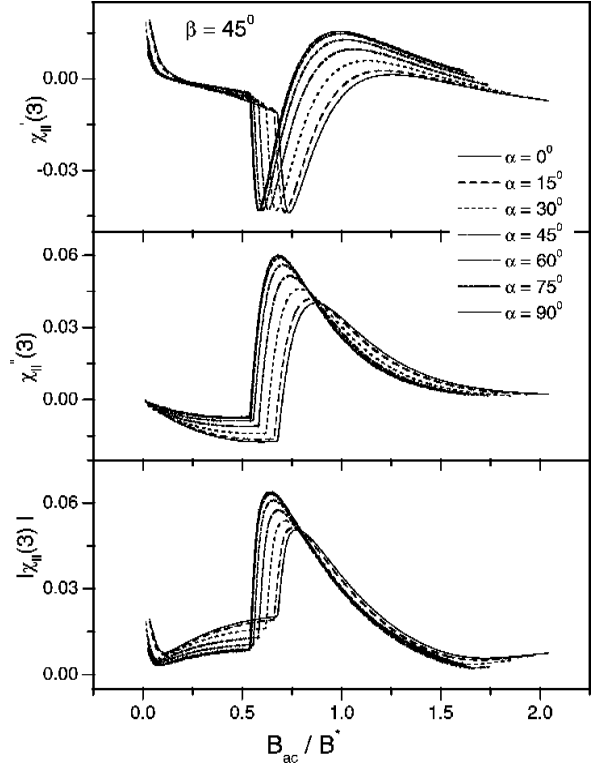


Figure 16. Real (χ'), imaginary (χ'') and modulus ($|\chi|$) of the parallel 3rd harmonics of ac susceptibility as a function of the normalized ac field amplitude for $\beta = 45^\circ$, α varying from 0° to 90° .

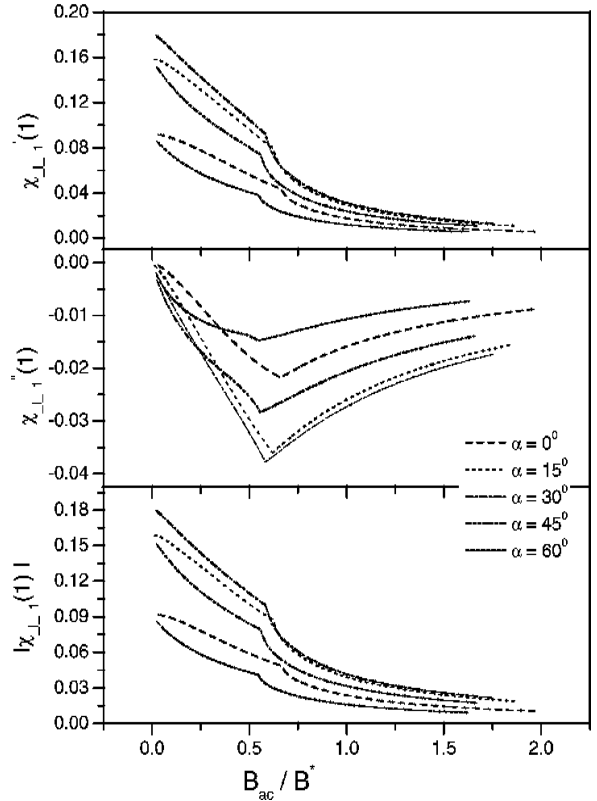


Figure 17. Real (χ'), imaginary (χ'') and modulus ($|\chi|$) of the first perpendicular fundamental ac susceptibility as a function of the normalized ac field amplitude for $\beta = 45^\circ$, α varying from 0° to 90° .

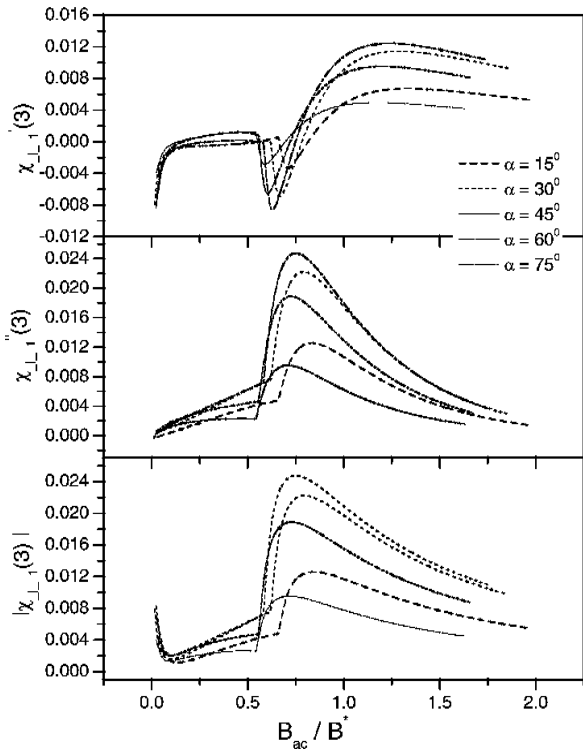


Figure 18. Real (χ'), imaginary (χ'') and modulus ($|\chi|$) of the first perpendicular 3rd harmonics of ac susceptibility as a function of the normalized ac field amplitude for $\beta = 45^\circ$, α varying from 0° to 90° .

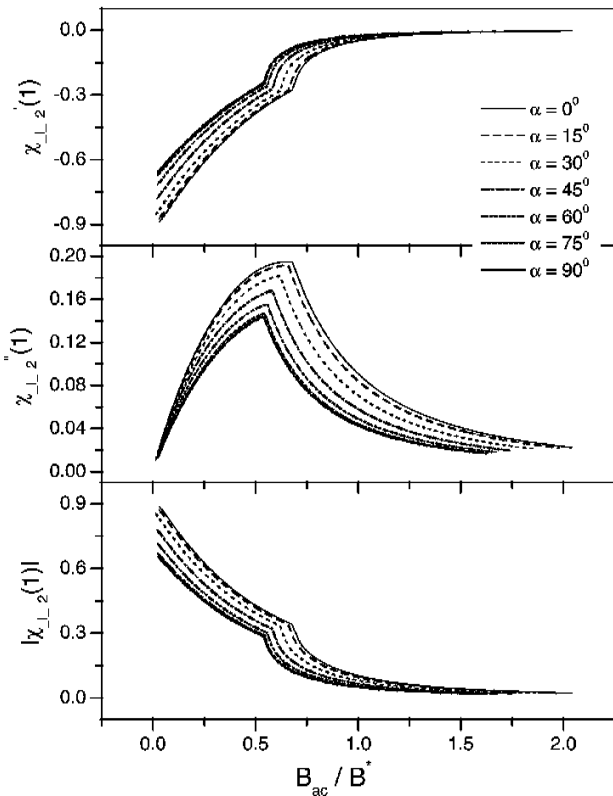


Figure 19. Real (χ'), imaginary (χ'') and modulus ($|\chi|$) of the second perpendicular fundamental ac susceptibility as a function of the normalized ac field amplitude for $\beta = 45^\circ$, α varying from 0° to 90° .

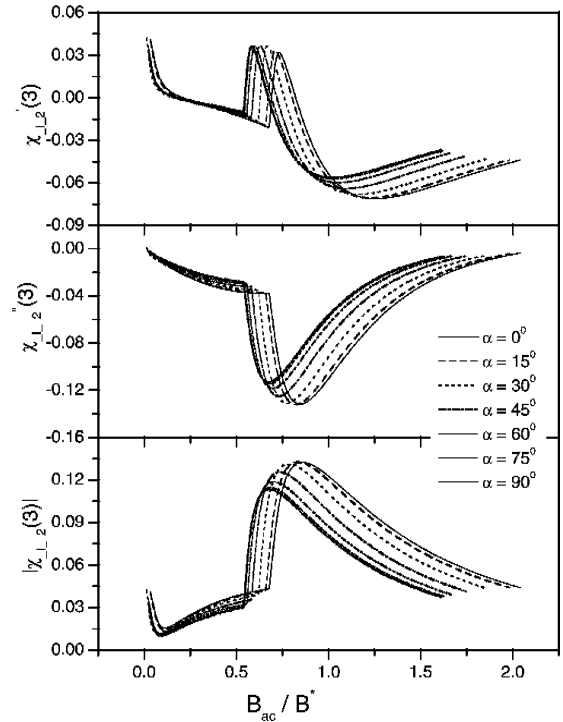


Figure 20. Real (χ'), imaginary (χ'') and modulus ($|\chi|$) of the second perpendicular 3rd harmonics of ac susceptibility as a function of the normalized ac field amplitude is plotted for $\beta = 45^\circ$, α varying from 0° to 90° .

cross section of the cylinder. Here, of course, we have presented only some selected figures (Figures 15–20) for illustration. For a detailed discussion, Refs. [39,40] can be consulted. For the general case $\beta = 45^\circ$, α varying from 0° to 90° , the fundamental and odd higher harmonics for the parallel and two perpendicular components upto 3rd order are plotted in Figures 15–20. We have also plotted the effects of geometric anisotropy for only parallel component with the change of a/b ratio for the rectangular cylinder. The variations are depicted in Figures 21(a) and (b). We compared our results with the experimental studies of [36] and [37] for silver-sheathed Bi-2223 tapes and MgB₂ polycrystalline bar respectively where a close resemblance can be observed.

5.3.6. Stepwise modification :

For all our earlier calculations, we have taken J_c to be field dependent. For analysis of the experimental results, the analytical formulation needs some more generalizations incorporating the field-dependence and stepwise modification of J_c .

This formulation is exactly similar to those followed in previous sections, where the volume current shell is constructed as a succession of infinitesimal shells, each considered as a surface current. As the applied field is in

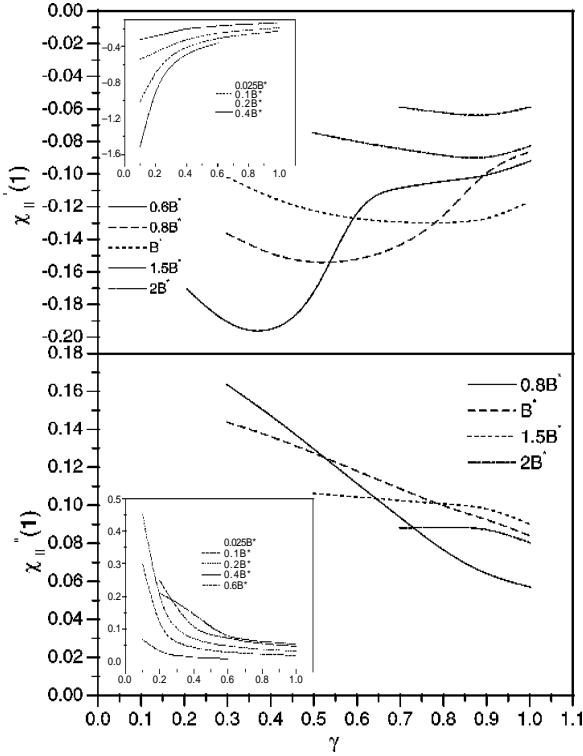


Figure 21. (a) Variation of $\chi_{||}'(1)$ with the aspect ratio ($\gamma = a/b$) of a cylinder with rectangular cross section for different values of the ac field amplitudes as indicated in the figure. Behaviour for low values of ac field amplitudes is depicted at the inset. (b) Variation of $\chi_{||}''(1)$ with the aspect ratio ($\gamma = a/b$) of a cylinder with rectangular cross section for different values of the ac field amplitudes as indicated in the figure. Behaviour for low values of ac field amplitudes is depicted at the inset.

the $x - y$ plane, the current density (surface as well as volume) is along z -axis. As $\mathbf{J}_s = J_s \hat{k}$, the relation between the surface and volume current density is given by :

$$J_s = \frac{J_v \chi d\xi}{|f'(\phi)|}. \quad (56)$$

Here, χ is the Jacobian of transformation from the variable (x, y) to (ξ, ϕ) as described in earlier sections. Equating the above equation with the surface current density expression, $J_s = 2\Gamma \delta B_a \sin(\gamma + \phi - \alpha) / |f'(\phi)|$, we obtain the volume current density as :

$$\mu_0 J_v = \frac{2\Gamma \sin(\gamma + \phi - \alpha)}{\chi} \frac{\delta B_a}{\delta \xi}. \quad (57)$$

Equating $|J_v| = J_c(B)$, we get :

$$\mu_0 J_c(B) \chi = \frac{\delta B_a}{\delta \xi} 2\Gamma \sin(\gamma + \phi - \alpha). \quad (58)$$

Let $\phi_0(\xi)$ be the value of ϕ where the transverse direction intersects the flux contour corresponding to ξ . Substituting $\phi = \phi_0$ in eq. (58) and denoting the corresponding value of χ by χ_0 we can express $\delta B_a / \delta \xi$ in terms of χ_0 .

$$\frac{\delta B_a}{\delta \xi} = \frac{\mu_0 J_c(B) |_{\phi=\phi_0} \chi_0}{2\Gamma \sin(\gamma + \phi - \alpha)}. \quad (59)$$

The right hand side of the above equation is known on a certain shell and can be expressed in terms of the coefficients of the conformal mapping (p_n and α_n) following a similar procedure as followed in earlier sections. Hence, knowing the right hand side of eq. (58) in terms of p_n and α_n , the derivatives p_n' and α_n' are obtained by solving the matrix equations. Thus, the next flux front can be constructed if one knows $J_c(B)$ on every point of the present shell. For this purpose, we obtain the local field by the formula

$$\mathbf{B}(\mathbf{r}) = \frac{\mu_0}{2\pi} \iint \frac{J_c(B) \chi(\xi', \phi') (-\hat{i}(y-y') + \hat{j}(x-x')) d\xi' d\phi'}{(x-x')^2 + (y-y')^2}. \quad (60)$$

Using eq. (58) one can rewrite the above equation as :

$$\mathbf{B}(\mathbf{r}) = \frac{1}{2\pi} \int_0^{B_a} \int_0^{2\pi} \times \frac{2\Gamma \sin(\gamma - \phi' - \alpha) (-\hat{i}(y-y') + \hat{j}(x-x')) d\phi' dB_a}{(x-x')^2 + (y-y')^2}. \quad (61)$$

Hence, the magnitude of the local field can be calculated as :

$$\mathbf{B} = \frac{1}{2\pi} \left[\left\{ \int_0^{B_a} \int_0^{2\pi} \frac{2\Gamma \sin(\gamma + \phi' - \alpha) (y-y') d\phi' dB_a}{(x-x')^2 + (y-y')^2} \right\}^2 + \left\{ \int_0^{B_a} \int_0^{2\pi} \frac{2\Gamma \sin(\gamma + \phi' - \alpha) (x-x') d\phi' dB_a}{(x-x')^2 + (y-y')^2} \right\}^2 \right]. \quad (62)$$

Calculating the local field, $J_c(B)$ can be calculated by using the appropriate functional form (exponential, Kim model, history dependence *etc.*) and hence the flux-front configuration or the magnetization calculation can be performed. The formulation is based on the realistic approach that each time with the change of the externally applied field, the local field inside the superconductor will be modified starting from the surface. This process of modification of the local field starting from the surface is similar as in the framework of the critical state model. On the other hand, our formulation contains some extra input in such a way that with any change of the external field, all the infinitesimal current shells (starting from the surface) get modified. This is different from our earlier

approach where (as J_c was constant) with an infinitesimal increase of applied field, only one innermost shell was added to the earlier flux front configuration (as all the other shells are already carrying a current J_c). In this case as J_c itself is field and sometimes history dependent, it gets modified for each shell with each and every infinitesimal changes in the external applied field. Such an approach of stepwise modification scheme is logically stronger from the realistic point of view and thus is very much useful to explain experimentally obtained results.

6. Class II problems

In this section, we shall address two unsolved problems of class II geometry, where the applied field direction is along the infinite dimension of the sample. In the first subsection, we study the effects of intrinsic anisotropy on the magnetization property of a hard type II material. In the next one, the order-disorder transition for a weakly pinned vortex matter system is studied.

6.1. Critical state model with anisotropic critical current density :

In the earlier sections, we obtained solutions of the CSM for cylindrical samples assuming an isotropic critical current density for $N \neq 0$ sample geometry. In this subsection, **analytical solutions of Bean's critical state model with anisotropic critical current density J_c are obtained for superconducting cylindrical samples of arbitrary cross section in a parallel geometry** [40] ($N = 0$ geometry). We present a method to calculate the flux fronts and magnetization curves.

CSM solutions are available in the literature [42,43,14,15,44,19,11,45], for field-independent as well as field-dependent J_c , for samples in parallel geometry where demagnetization factor $N = 0$ as also for perpendicular geometry where $N \neq 0$. In all these solutions, the critical current density is assumed to be **isotropic**, *i.e.* $|J_c|$ does not depend on the orientation of J_c . Although the assumption of isotropy is valid for many real samples, there are situations where the assumption cannot be justified, *e.g.* samples of high- T_c superconductors with field parallel to ab -plane [46] and also [47] for the newly discovered superconductor MgB_2 when the applied field is inclined to the c -axis. Schuster *et al* [48] have studied flux penetration into thin rectangular samples having anisotropic critical current density in the perpendicular geometry. This geometry pertains to $N \neq 0$. Here, the effects of anisotropy are

compounded with those due to a non-zero demagnetization factor. To study the effects of anisotropy alone, it would be instructive to analyze the problem for the $N = 0$ geometry. In the present study, we consider **cylindrical samples of hard type-II superconductors in a parallel geometry**. The simple geometry brings out the essential features of anisotropy in J_c and, moreover, is amenable to an analytical treatment.

In next subsection, we briefly present the formulation and a derivation of the general form of flux-fronts assuming arbitrary cross section for the cylinder and also an arbitrary form of the anisotropy in J_c . This should suffice for the calculation of magnetization curves. However, for purpose of illustration, we choose elliptic cylindrical samples and the elliptic form [49] of anisotropy for J_c .

6.1.1. Formulation :

Consider an infinite cylindrical sample of a hard type-II superconductor subjected to a magnetic field B_a parallel to its axis that is taken to be z -axis (Figure 22). The

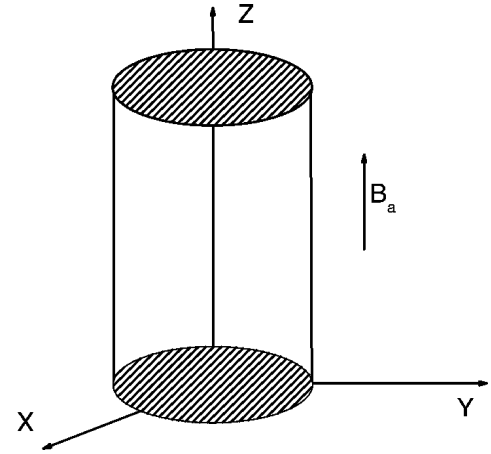


Figure 22. The parallel geometry for a cylindrical sample. The cylinder is infinite in tz -direction. The long axis of the cylinder is parallel to the z -axis, which is also the direction of the applied field B_a .

magnetic field B within the sample is determined from the equations :

$$\partial B / \partial x = -\mu_0 J_y, \quad \partial B / \partial y = \mu_0 J_x, \quad (63)$$

where J_y and J_x are components of the shielding current density and satisfy the condition of the CSM, $J_y^2 + J_x^2 = |J_c|^2$. To study the effect of anisotropy in J_c , we assume the general form

$$|J_c| = J_{c0} f(\theta). \quad (64)$$

Here θ refers to the direction of the current density, *i.e.*

tan $\theta = J_x/J_y = -(\partial B/\partial y)/(\partial B/\partial x)$, and J_{c0} is the critical current density in the absence of anisotropy. In general, J_{c0} could be a known function of the local field \mathbf{B} , say, $J_{c0}(\mathbf{B})$. From eqs. (63) and (64), we have

$$(\partial B/\partial x)^2 + (\partial B/\partial y)^2 = (\mu_0 J_c)^2 = (\mu_0 J_{c0})^2 f(\theta)^2. \quad (65)$$

Solution of eq. (65) determines the function $\mathbf{B}(x, y)$, that assumes the value B_a on the boundary, gives the distribution of the local field within the sample. It also determines the contours of constant B or the flux fronts. Before we determine the flux contours, following [50], let us introduce a new variable say β , with the dimension of length. In [50], the indefinite integral

$$\beta = \int^B dv / [\mu_0 J_{c0}(v)].$$

was used. We shall work with the definite integral representation of β with zero as the lower limit. If we determine β , we can obtain $\mathbf{B} = \mathbf{B}(\beta)$ by inverting the above defining equation. We shall also denote by β_a the β -value corresponding to B_a , i.e. $\mathbf{B}_a = \mathbf{B}(\beta_a)$. Further, we will assume that $J_{c0}(\mathbf{B})$ is a monotonically decreasing function of $|B|$. Thus, flux contours can be determined from the knowledge of either B or β . The latter satisfies the equation

$$(\partial B/\partial x)^2 + (\partial B/\partial y)^2 = f(\theta)^2. \quad (66)$$

A comparison of eq. (66) (that does not involve $J_{c0}(\mathbf{B})$) with eq. (65) shows that the shape of the flux fronts is independent of the functional dependence of $J_{c0}(\mathbf{B})$. If J_{c0} is independent of \mathbf{B} then β and B are linearly related by $B = \mu_0 J_{c0} \beta$. It would be prudent to work with eq. (66) rather than eq. (65). Clearly, eq. (66) is a nonlinear first order partial differential equation. Its solution can be obtained [51] as an *envelope of its one parameter family of solutions*, which in turn, is obtained from its *complete integral*, i.e. a solution involving two arbitrary constants. It is easy to see that the function

$$\beta = px + qy + r \quad (67)$$

involving parameters p , q and r that are independent of x and y , satisfies eq. (65) provided

$$p^2 + q^2 = f(\theta)^2 \quad (68)$$

with tan $\theta = -q/p$. Thus, p and q are related. If we choose the parameter r also as a function of p , we get a one parameter family of solutions of eq. (65). Alternatively, we choose a parameter ϕ and write $p = \rho \cos \phi$ and $q = \rho \sin \phi$ and set $r = r(\phi)$. We then have

$\theta = -\phi$, and if we choose $\rho = f(\phi)$, eq. (68) reduces to an identity. In terms of the parameter ϕ , eq. (65) may be written as

$$\beta = \rho(\cos \phi + \sin \phi) + r(\phi). \quad (69)$$

For a fixed value of β , eq. (69) represents a plane in the (β, x, y) space. The envelope of the one parameter family of planes represented by eq. (69) is obtained as usual by eliminating ϕ between eq. (69) and the equation

$$0 = \rho'(x \cos \phi + y \sin \phi) + r'(\phi) + \rho(-x \sin \phi + y \cos \phi) \quad (70)$$

obtained by differentiating eq. (69) with respect to the parameter ϕ . In the above equation, prime on a symbol denotes the derivative with respect to ϕ . The solution surface (envelope of surfaces represented by eq. (69)) must touch every member of the family. Thus, each point on the solution surface corresponds to some value of ϕ . Let us take $x = x(s)$, $y = y(s)$ to be the parametric equations for the boundary of the cross section of the cylindrical sample. The solution will satisfy the boundary condition if $\beta(x(s), y(s)) = \beta_a$, is identically satisfied for all values of the parameter s . Hence, $\partial \beta(x(s), y(s))/\partial s$ must vanish for all s . These two requirements determine which member of the family touches the solution surface at the point $(\beta_a, x(s), y(s))$, i.e. determines ϕ as a function of s and also the unknown function $r(\phi)$. From eqs. (69) and (70), we have

$$r(\phi) = \beta_a - \rho(x(s) \cos \phi + y(s) \sin \phi), \quad (71)$$

$$0 = \rho'(x(s) \cos \phi + y(s) \sin \phi)$$

$$r'(\phi) + \rho(-x(s) \sin \phi + y(s) \cos \phi), \quad (72)$$

valid for all s . Differentiating eq. (71) with respect to s yields

$$\cos \phi(dx/ds) + \sin \phi(dy/ds) = 0. \quad (73)$$

Eq. (73) provides the relation between ϕ and s , i.e. it determines which member of the family touches the solution surface at the point $(x(s), y(s))$. Eqs. (69–72) imply

$$\beta - \beta_a = \rho[(x - x(s)) \cos \phi + (y - y(s)) \sin \phi] \quad (74)$$

and

$$0 = \rho'(x - x(s)) \cos \phi + (y - y(s)) \sin \phi + \rho[-(x - x(s)) \sin \phi + (y - y(s)) \cos \phi]. \quad (75)$$

Using the relation $\rho = f(\phi)$ and solving eqs. (74) and (75) for x and y , we get the parametric equations for the constant B or the flux contours

$$x = x(s) - (h/\rho)[(\rho'/\rho)\sin\phi + \cos\phi], \quad (76)$$

$$y = y(s) - (h/\rho)[\sin\phi - (\rho'/\rho)\cos\phi]. \quad (77)$$

It should be noted that during the virgin curve, $B > 0$ and progressively decreases towards the center of the sample and hence for all $J_{c0}(\mathbf{B})$ decreasing with $|\mathbf{B}|$, $\beta - \beta_a$ is negative, while during field reversal from the field increasing case, $\beta - \beta_a$ is positive over part of the sample. To cover both these cases, we have used $h = |\beta - \beta_a|$ in eqs. (76) and (77). The entire sample can be covered by means of flux contours if h is allowed to vary from $h = 0$ at the surface to $h = B_p$, at the field for full penetration.

Since we have solved eq. (66), we should remember that the flux-contour parameter $h = |\beta - \beta_a|$ involves β . In the case of constant J_{c0} , $B = \mu_0 J_{c0} \beta$ and $B_a = \mu_0 J_{c0} \beta_a$. In the general case of field, dependent J_{c0} , B is obtained from β by inverting the defining equation for β based on the known field dependence of J_{c0} . Eqs. (76) and (77), together with eq. (73) that expresses a relation between ϕ and s , represent the general result for flux fronts valid for cylindrical samples of any arbitrary cross section whose boundary is represented by the parametric functions $x = x(s)$, and $y = y(s)$ and for an arbitrary form of anisotropy. In principle, virgin and hysteresis magnetization of the sample can be obtained using these equations. We shall now specialize these equations to elliptic cylinders and elliptic form of anisotropy.

6.1.2. Elliptic cylinder and elliptic anisotropy :

(a) The flux contours :

The elliptic boundary of the sample (the boundary of the transverse cross section of the cylinder) may be represented by the parametric equations

$$x(s) = a \cos s, \quad y(s) = b \sin s. \quad (78)$$

The semi-axes of the ellipse are denoted by a and b , respectively. Without loss of generality, we may assume $a > b$. To describe the anisotropy of J_c we choose in eq. (64) the following (elliptic) form of $f(\theta)$:

$$f(\theta) = (\cos^2 \theta + \alpha^2 \sin^2 \theta)^{1/2}. \quad (79)$$

Using eq. (79) in (73), we get the relation between s and ϕ : $\tan s = (b/a) \tan \phi$. We now express eqs. (76) and (77) that govern the shape of the flux fronts in terms of ϕ :

$$x = \left[(a^2 / \Delta) - (h / \rho) \{ 2 - 1 / \rho^2 \} \right] \cos \phi, \quad (80)$$

$$y = \left[(b^2 / \Delta) - (h / \rho) \{ 2 - (a / \rho)^2 \} \right] \sin \phi, \quad (81)$$

where

$$\Delta = (a^2 \cos^2 \phi + b^2 \sin^2 \phi)^{1/2}, \quad (82)$$

$$\rho = f(\phi) = (\cos^2 \theta + \alpha^2 \sin^2 \theta)^{1/2}. \quad (83)$$

It should be remarked that eqs. (80) and (81) represents mathematical flux fronts which can possibly have double points corresponding to applied field beyond a certain value [42,50]. The physically acceptable flux fronts must progressively reduce in size and can be obtained from the mathematical flux fronts by dropping out the extraneous portions. Figure 23 should clarify the situation. Figure 23(a) shows the mathematical flux fronts and Figure 23(b) shows the physically acceptable ones obtained from Figure 23(a). Eqs. (80) and (81) also determine B_p , the field for full flux penetration. At full penetration, the flux contour reduces to a point (the center of the sample) or a line that must pass through the center of the sample. At full penetration, the point $x = y = 0$ lies on the flux contour. A simple algebra using eqs. (80), (81), (82) and (83), leads to the result that h_p

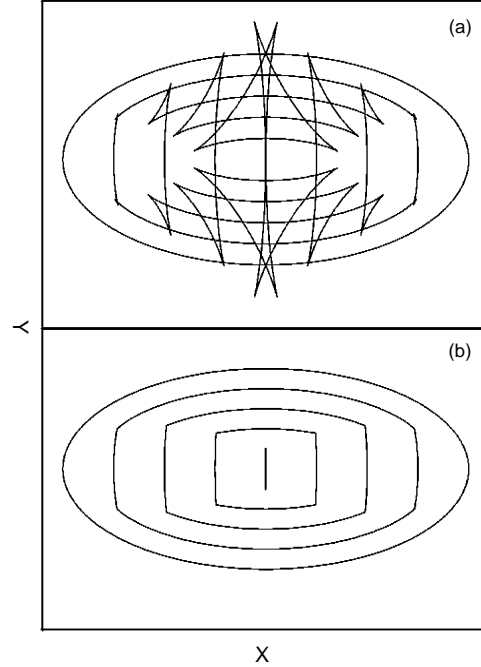


Figure 23. (a) Typical flux contours represented by eqs. (13). The outermost is the sample boundary of the elliptical cross section of the cylinder with semi axes $a = 1$ and $b = 0.5$. The next one just begins to have double points. All the other contours have visible loops at the double points. These are mathematical solutions. (b) The physically acceptable flux contours obtained from those in (a) by removing the loops at the double points. The anisotropy parameter $\alpha = 2.5$.

$= |\beta_p - \beta(0)| = \min(a, b\alpha)$, where $\min(u, v)$ stands for the smaller of u and v ; β_p is the β -value corresponding to the applied field B_p , $B_p = B(\beta_p)$. Hence B_p can be determined.

(b) *Magnetization curves :*

The magnetization of the sample is calculated using the definition

$$\begin{aligned} \mu_0 m &= (1/A) \int (B - B_a) dx dy \\ &= -B_a + (1/A) \int B dx dy . \end{aligned} \quad (84)$$

Integration is performed over the cross sectional area A of the sample. Let us first consider magnetization during the virgin curve for a zero field-cooled sample. For this case, we have $\beta - \beta_a = -h$. On the sample surface $B = B_a$, hence, $h = 0$. Similarly, on and within the innermost flux contour $B = 0$ implying $h = B_a$. It is advantageous to change the variables of integration from (x, y) to (h, ϕ) as per eqs. (80) and (81). For a given applied field B_a , variation of h may be restricted only to the range $(0, \beta_a)$ beyond which $B = 0$. The surface elements are related through J , the Jacobian of the transformation, and can be calculated in a straightforward manner; the result is

$$\begin{aligned} J(h, \phi) &= h \left[(3\alpha^2 / \rho^6) - \{2(1 + \alpha^2) / \rho^4\} \right] \\ &+ a^2 b^2 / \Delta^3 \rho . \end{aligned} \quad (85)$$

The virgin magnetization can be written as

$$\begin{aligned} \mu_0 m_v &= -B_a + (1/A) \int B J dh d\phi \\ &= -B_a - \frac{1}{\pi a b} \int_0^{\beta_a} dh B(\beta_a - h) \int J d\phi . \end{aligned} \quad (86)$$

Using the values of integrals in the expression (86) for virgin magnetization and the expression (85) for J we have calculated the virgin magnetization. It reaches its saturation value m_s at the field B_p for full penetration. For $B_a > B_p$, $m_v = m_s$.

Magnetization under reversal of field from some field B_m can be expressed in terms of virgin magnetization. Let us denote $m_v(B_a)$, the functional form for the virgin magnetization. On the virgin curve, for $B_a = B_m$, $m = m_v(B_m)$. Let the applied field be now reduced to say, $B_a = B_m - \Delta B$. The shielding currents near the surface region will reverse their sense of flow, so as to shield the interior from the change of field $-\Delta B$. Hence, we can

write magnetization under field reversal $m_v(B_m - \Delta B) = m_v(B_m) - 2m_v(\Delta B)$. We can increase $-\Delta B$ up to B_m corresponding to applied field decreased to $-B_m$. To complete the loop the field is increased from $-B_m$ to B_m . The magnetization during the field increasing part of the loop is obtained using $m_v(B_a) = -m_v(-B_a)$.

(c) *Field dependent critical current density :*

The calculation of magnetization presented above is directly applicable to the case of constant critical current density. As remarked earlier, field dependence of J_c does not alter the shape of flux contours. It should be remembered that, in the general case of field dependent J_c , the flux contours are labeled by the parameter $h = |\beta_a - \beta|$, with β as defined earlier. The above formulae for magnetization can be utilized with this identification and using the appropriate expression for $(\beta - \beta_a)$ in eq. (86). For the exponential model, we have $J_{c0} = J_{c0}(0) \exp(-|B|/B_0)$, where B_0 is a parametric field that governs the decay of the current density. For definiteness, we calculate β from the definition

$$\beta = \int_0^B dv / [\mu_0 J_{c0}(v)] = \pm \frac{B_0}{\mu_0 J_{c0}} (\exp(|B|/B_0) - 1). \quad (87)$$

Thus for the virgin curve we have both $B > 0$ and $B_a > 0$, and we have

$$\beta_a = (B_0 / \mu_0 J_{c0}) [\exp(B_a / B_0) - 1],$$

$$\beta = (B_0 / \mu_0 J_{c0}) [\exp(B / B_0) - 1],$$

and consequently,

$$h = (B_0 / \mu_0 J_{c0}) [\exp(B_a / B_0) - \exp(B / B_0)], \quad (88)$$

or equivalently,

$$B = B_0 \ln [\exp(B_a / B_0) - (\mu_0 J_{c0} h / B_0)]. \quad (89)$$

The flux-contour parameter h increases from 0 to its maximum value β_a , corresponding to $B = 0$. Eq. (89) determines B in terms of h for $h < \beta_a$. For $h > \beta_a$, $B = 0$. Virgin magnetization can be determined from eq. (86). Virgin curve extends even beyond the field B_p corresponding to full penetration. Since $B > 0$ everywhere, the B -profile is given by eq. (89). This part of the virgin curve merges with the field increasing envelope curve obtained below.

During the envelope curve, shielding, currents flow throughout the sample in one sense. On the field-increasing envelope, the local field B decreases towards

the center of the sample. If we write $\beta_p = (B_0/\mu_0 J_{c0}) [\exp(B_p/B_0) - 1]$ corresponding to field for full penetration, we have three situations, viz. (i) $B_a < 0$, (ii) $0 < B_a < B_p$ and (iii) $B_a > B_p$. Calculating the local field in all these three regions, we can plot the hysteresis loops for the sample.

(d) Summary and discussion :

We have presented a general method to obtain flux contours and magnetization curves for cylindrical samples of arbitrary cross section, in parallel geometry, with anisotropic critical current density. The method is applied to cylindrical samples of elliptical cross section and an elliptic form of the anisotropy.

Mathematical solutions to flux contours develop double points. We have presented a prescription to locate the double point and get physically acceptable flux contours. Figure 23 illustrates the procedure for an elliptical cylinder with semi axes $a = 1$ and $b = 0.5$ and the anisotropy parameter $\alpha = 2.5$. Detailed calculations of elimination of the extraneous portions are presented in Ref. [41]. An important outcome of this study reveals that for a certain range of the anisotropy parameter, there is no distinction between the flux fronts obtained for the isotropic and anisotropic samples. It is seen that, for $\alpha < 1$ but $a\alpha > b$ the character of the flux contours is similar to those in an isotropic sample with $b < a$. Figure 24 illustrates this fact.

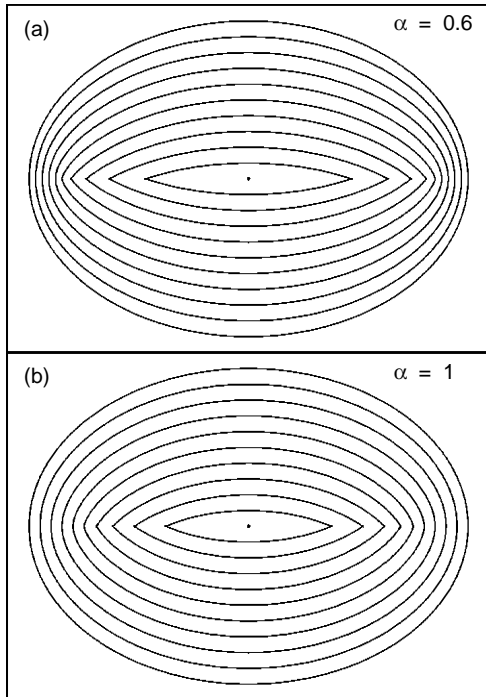


Figure 24. (a) Flux contours for the elliptical cylinder, with semi axes $a = 1$ and $b = 0.5$ with (a) $\alpha = 0.8$ and (b) for the isotropic sample i.e. $\alpha = 1$.

The effect of anisotropy would be best brought out if the sample is symmetric. For a circular cylinder of radius $a = 1$, flux contours are plotted in Figure 25 for two values of the anisotropy parameter $\alpha = 2.5$ and 0.6 . For the isotropic case ($a = 1$), it is well known that the flux contours are concentric circles. There is a qualitative change in the shape of the flux contours for $a \neq 1$. It is seen that Figure 25(b) is qualitatively similar to Figure 22(b), while Figure 25(a) is similar to 25(b) rotated by 90° . The manner the flux contours evolve, as field

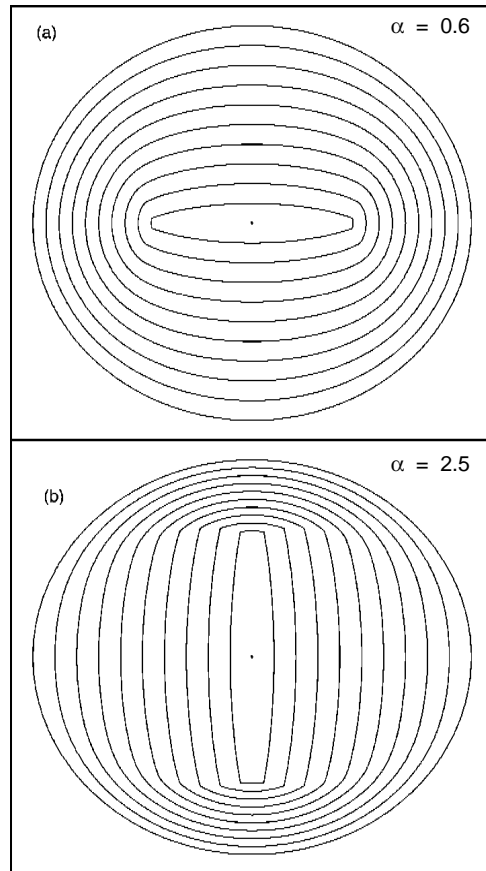


Figure 25. A comparison of flux contours for a circular cylinder with (a) $\alpha = 2.5$ and (b) $\alpha = 0.6$.

penetrates the sample, is different for the two cases $a > 1$ to $a < 1$ as seen from Figure 25. This is to be expected from the θ dependence of $|J_c|$ and keeping in mind that higher value of $|J_c|$ leads to less penetration.

Virgin magnetization curves are presented in Figure 26 for anisotropic critical current density that decays exponentially with the local field, for three values of the anisotropy parameter α . A comparison of magnetization hysteresis loops is presented in Figure 27. Here we plot the virgin curve, the envelope curves and the reversal curves for various reversal fields. The size of the hysteresis loop increases with α .

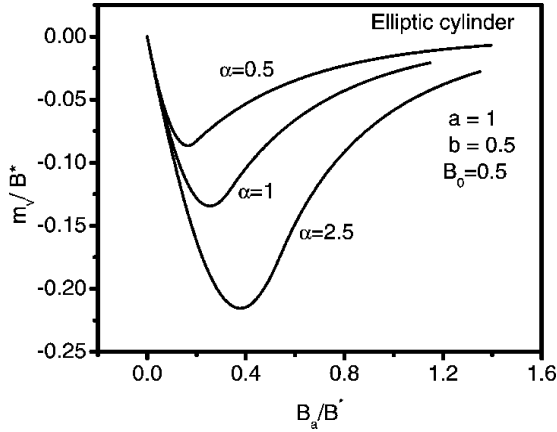


Figure 26. Virgin curves for the exponential model $J_{c0} \sim \exp(-|B|/B_0)$ with $B_0 = 0.5B^*$, where $B^* = \mu_0 J_{c0} a$, for different values of the anisotropy parameter α . The elliptical cylindrical sample has semi axes $a = 1.0$ and $b = 0.5$.

For thin samples, to first order in (d/L) (d is the thickness and L is the lateral dimension transverse to the applied field), the effect of anisotropy in the critical current density can be taken into account by an effective field-dependence of the critical current density [52]. For cylindrical samples and elliptical form of the anisotropy treated here, such a replacement is not possible. Thus, the fortunate circumstance mentioned above, does not hold for thick samples.

Finally, the case of elliptical cylindrical samples and the elliptic anisotropy was chosen for purpose of illustration and the method presented is applicable to cylinders in general and for other forms of anisotropy in J_c . The method was also applied to cylinders of rectangular cross section. For rectangular cylinders, we found that (in a parallel geometry) shape dominates anisotropy in that the flux contours are similar to those for an isotropic rectangular cylinder.

6.2. Studies of order-disorder transitions in weakly pinned vortex matter systems :

Vortex matter system provides an excellent opportunity to study the combined effect of disorder and thermal fluctuations on a system having crystalline order. In the mixed state of type-II superconductors, just above H_{c1} , pinning dominates over the inter-vortex interaction and hence a highly disordered flux-line lattice (FLL) results. With gradual increase of the applied field, more and more vortices penetrate inside and a growing inter-vortex interaction initially leads to the formation of quasi-ordered Bragg glass (BG) phase. In this particular ordered phase, elastic energy of the FLL dominates. This disorder-order transition in the low field [53,54], depends on the average

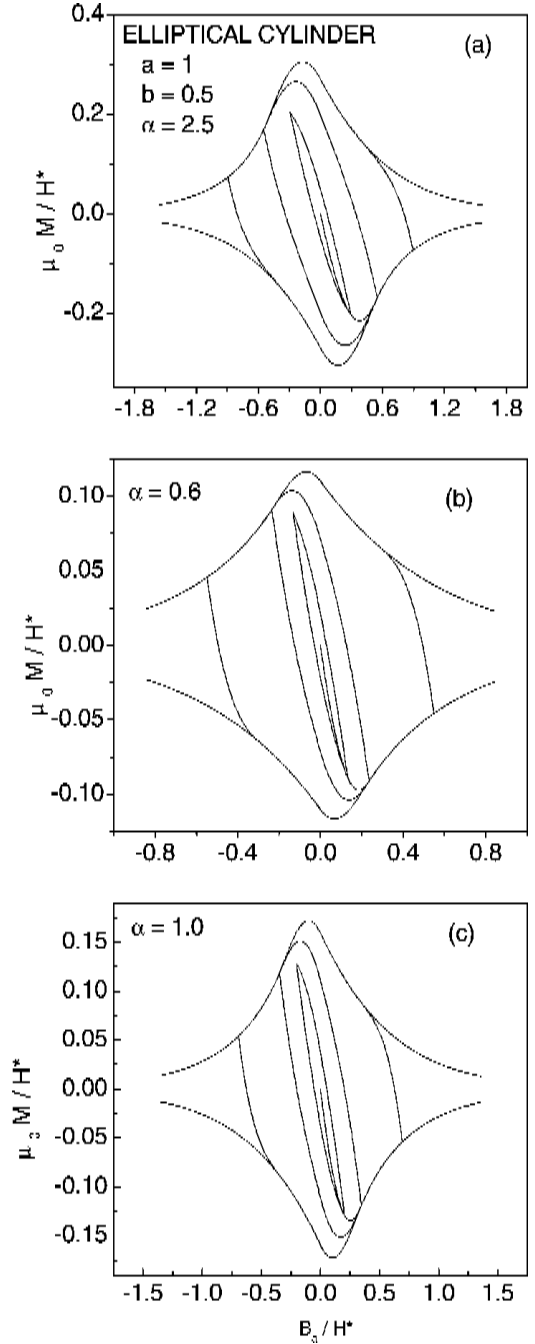


Figure 27. Virgin curve and the envelope curves for elliptical cylinder with semi axes $a = 1.0$ and $b = 0.5$ and the exponential model for J_c . (a) For $\alpha = 2.5$, the field for full penetration $B_p = 0.549B^*$. The small and large hysteresis loops are also shown corresponding to the reversal fields $B_m = 0.2939B^*$, $B_m = B_p$ and $B_m = 0.8959B^*$ respectively. (b) Same as (a) for $\alpha = 0.6$. For this case $B_p = 0.235B^*$ and the reversal fields are $B_m = 0.1312B^*$, $B_m = B_p$ and $B_m = 0.5148B^*$. (c) We also show hysteresis curves for a symmetric sample ($\alpha = 1$) for comparison. For this case $B_p = 0.3466B^*$ and the reversal fields are $B_m = 0.2027B^*$, $B_m = B_p$ and $B_m = 0.6931B^*$.

pinning force within the superconductor system. With further increase of field, BG phase undergoes another transition to a highly disordered phase due to the increased softening of the lattice [53]. Following Larkin-

Ovchinnikov's collective pinning theory [55], this high field order-disorder transition leads to a sharp decrease in the correlation volume of FLL and hence results in a steep rise in the critical current, known as the peak effect for the conventional superconductors and second magnetization peak for high temperature superconductors. Basically, this peak in J_c occurs in a regime, where the pinning energy becomes comparable with inter-vortex interaction. This whole process is depicted in Figure 28(a). More complicated details of the phase diagram are discussed in Ref. [56]. This high field order-disorder transition is characterized by vortex state metastability and pronounced history dependence in J_c . A wide variety of studies deal with the disorder-induced metastability of vortex matter systems [53,54].

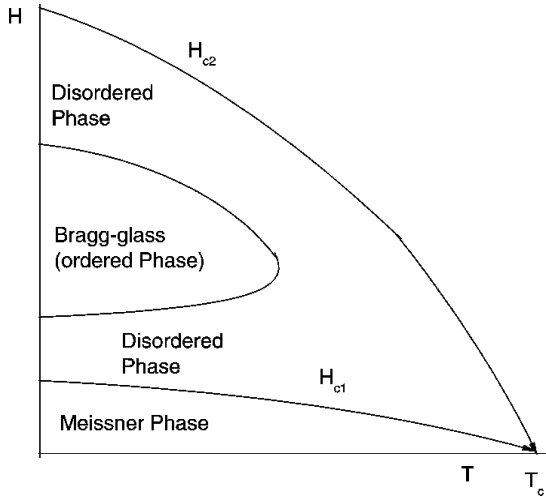


Figure 28(a). Conceptual H-T phase diagram in the mixed state of a type-II superconductor depicting the Bragg glass and disordered solid phases. The boundary of the Bragg glass phase represents the low and high field order-disorder transition lines.

In this subsection, we deal with the history dependence of J_c and its effects on the minor curves of magnetization and magnetostriction. Usually, the history dependence of J_c is investigated by means of minor magnetization curves. Some interesting features of minor magnetization curves manifesting the history dependence of J_c are :

- (i) Near the onset of peak effect, the minor curves starting on the field increasing envelope saturate (undershoot) inside the field decreasing envelope and asymptotically meet the envelope only at much lower fields. On the other hand, minor curves starting on the field decreasing envelope overshoot the forward curve. This implies that near the onset of peak effect, J_c is larger on the field decreasing

envelope than on the field increasing one. However, close to the peak field (B_p), the minor curves merge with the envelope and hence J_c is history independent.

- (ii) Behaviour of the minor curves near the low field order-disorder transition is exactly opposite to that in the high field case. Here, the minor curves starting on the field increasing envelope overshoot the field decreasing one and those starting on the reverse curve undershoot the forward one. Hence, J_c is larger on the increasing field branch than on the decreasing field branch. These features will be more clear from minor curves presented in [57].

6.2.1. Formulation for infinite slab geometry :

Let us consider a slab having infinite extent along the y and z direction and with a thickness $2a$ along the x -direction. The sample geometry is as shown in Figure 2.

The field profile within the slab is governed by the critical-state equation :

$$\partial B(x, B_a) / \partial x = \pm \mu_0 J_c(B), \quad (90)$$

where the positive and the negative signs stand for the field decreasing and increasing cases, respectively. We briefly describe some of the steps leading to the final equation from the Ref. [58]. With an infinitesimal change δB_a of the external applied field, the above equation becomes :

$$\partial B(x, B_a \pm \delta B_a) / \partial x = \pm \mu_0 J'_c(B) \quad (91)$$

with $J'_c(B) = J_c + |\Delta B| B_r (J^{\text{st}} - J_c)$. Here, B_r is a field dependent parameter. This modified critical current density contains the effect of history-dependence through the second term. In the conventional Critical State Model approach, the change in the $J_c(B)$ is totally governed by the change in the local field. However, close to the order-disorder transition, there can be various metastable configurations for the vortex matter. Among all of them, the stable equilibrium configuration is associated with the current density J^{st} . Transition from one metastable state to another, one can be induced by a change in the field driving the system towards the stable configuration as indicated in the expression of J'_c . Hence, difference of eqs. (91) and (90) results :

$$\partial |\Delta B| / \partial x = \frac{|\Delta B|}{B_r} \left[\mu_0 J^{\text{st}} \pm \partial B(x, B_a) / \partial x \right]. \quad (92)$$

At first, we bring out the detailed features of the high

field order-disorder transition by assuming a simple single step function type behaviour for J^{st} as shown in Figure 28(b).

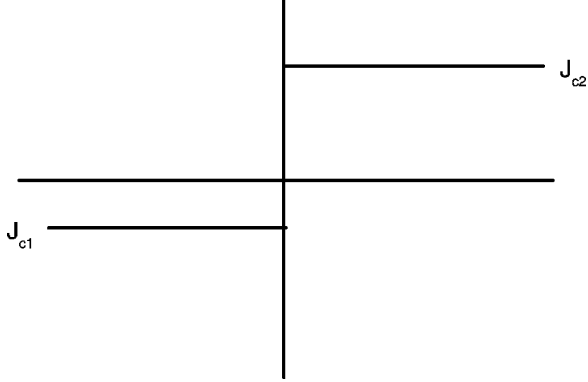


Figure 28(b). Single-step function behaviour of the current density representing the high-field order-disorder transition.

$$\begin{aligned} J^{\text{st}} &= J_1 \text{ for } B_a < B_0, \\ &= J_2 \text{ for } B_a > B_0. \end{aligned} \quad (93)$$

Eq. (92) can be solved with the boundary condition at $x = 0$, $|\Delta B| = \delta B_a$ leading to the equation determining the evolution of the field profile :

$$\begin{aligned} \partial B(x, B_a) / \partial B_a \\ = \exp \left\{ \left[-\mu_0 \int J^{\text{st}} dx \pm \{B(x, B_a) - B_a\} \right] / B_r \right\}. \end{aligned} \quad (94)$$

The above equation can be solved with appropriate boundary conditions to obtain the field decreasing (positive sign) and field increasing (negative sign) envelopes. We denote the field profiles for the increasing and decreasing case by $B \uparrow(x, B_a)$ (or $B \uparrow$, in short), and $B \downarrow(x, B_a)$ (or $B \downarrow$, in short), respectively.

(a) *Field increasing envelope (forward curve) :*

For the forward curve, the initial profile at any point x is given by :

$$B \uparrow(x, B_a) = B_s \uparrow - \mu_0 J^{\text{st}} x. \quad (95)$$

This is obvious from the negative slope straight line showing a field increasing profile beyond full penetration. Eq. (94) for the field increasing case becomes :

$$\begin{aligned} \partial B \uparrow / \partial B_a \exp(B \uparrow / B_r) \\ = \exp \left\{ \left(B_a - \mu_0 \int J^{\text{st}} dx \right) / B_r \right\} \\ = \exp \left\{ \left(B_a - \mu_0 J_1 x \right) / B_r \right\} \Theta(B_a - B_0) \\ + \exp \left\{ \left(B_a - \mu_0 J_2 x \right) / B_r \right\} \Theta(B_a - B_0). \end{aligned} \quad (96)$$

Integrating both sides of the above equation from $B_s \uparrow$ to $B \uparrow$, the expression for the local field for the forward curve can be obtained from :

$$\begin{aligned} \exp(B \uparrow / B_r) &= \exp(B_s \uparrow / B_r) \\ &+ \exp(-H_1^* r / B_r) \left\{ \exp(B \uparrow / B_r) \Theta(B_0 - B \uparrow) \right. \\ &- \exp(B_s \uparrow / B_r) \Theta(B_0 - B_s) + \exp(B_0 / B_r) \\ &\times \left. \left(\Theta(B_0 - B_s) - \Theta(B_0 - B \uparrow) \right) \right\} \\ &+ \exp(-H_2^* r / B_r) \left\{ \exp(B \uparrow - B_r) \Theta(B \uparrow / B_0) \right. \\ &- \exp(B_s \uparrow / B_r) \Theta(B_s - B_0) \\ &- \left. \exp(B_0 / B_r) \left(\Theta(B \uparrow - B_0) - \Theta(B_s - B_0) \right) \right\}, \end{aligned} \quad (97)$$

where $H_1^* = \mu_0 J_1 a$ and $H_2^* = \mu_0 J_2 a$. With the expression for the local field, the magnetization of the infinite slab is calculated as :

$$\mu_0 m = \frac{1}{a} \int_0^a B(x) dx - B_a. \quad (98)$$

(b) *Field decreasing envelope (reverse curve) :*

For the reverse curve, the initial profile at any point x is given by :

$$B \downarrow(x, B_a) = B_m \downarrow + \mu_0 J^{\text{st}} x. \quad (99)$$

This is obvious from the positive slope straight line showing a field decreasing profile beyond full penetration. Eq. (94) for the field decreasing case becomes :

$$\begin{aligned} \partial B \downarrow / \partial B_a (-B \downarrow / B_r) \\ = \exp \left\{ \left(-B_a - \mu_0 \int J^{\text{st}} dx \right) / B_r \right\} \\ = \exp \left\{ \left(-B_a - \mu_0 J_1 dx \right) / B_r \right\} \Theta(B_0 - B_a) \\ + \exp \left\{ \left(-B_a - \mu_0 J_2 dx \right) / B_r \right\} \Theta(B_a - B_0). \end{aligned} \quad (100)$$

Integrating both sides of the above equation from $B_m \downarrow$ to $B \downarrow$, the expression for the local field for the reverse curve can be obtained from :

$$\begin{aligned} \exp(-B \downarrow / B_r) &= \exp(-B_m \downarrow / B_r) \\ &- \exp(-H_1^* r / B_r) \left\{ -\exp(-B \downarrow / B_r) \Theta(B_0 - B \downarrow) \right. \\ &+ \left. \exp(-B_m \downarrow / B_r) \Theta(B_0 - B_m) \right\} \end{aligned}$$

$$\begin{aligned}
& -\exp(-B_0/B_r) \left(\Theta(B_0 - B_m) - \Theta(B_0 - B \downarrow) \right) \Big\} \\
& + \exp(-H_2^* r / B_r) \left\{ -\exp(-B \downarrow / B_r) \Theta(B \downarrow - B_0) \right. \\
& + \exp(-B_m \downarrow / B_r) \Theta(B_m - B_0) \\
& \left. - \exp(-B_0 / B_r) \left(\Theta(B \downarrow - B_0) + \Theta(B_m - B_0) \right) \right\}.
\end{aligned} \tag{101}$$

(c) *Reversal from the field decreasing envelope :*

We now get the profiles under reversal of the field. Let us consider reversal from a point on the upper envelope with the applied field B_m . We consider three regions. In the first one $0 < x < p$, the evolution of profiles is governed by eq. (94) with a negative sign. In the next one, $p < x < p + \delta p$,

$$\partial B \downarrow (x, B_m) / \partial x = \mu_0 J_c(B) \tag{102}$$

and

$$\partial B \uparrow (x, B_a + \delta B_a) / \partial x = \pm \mu_0 J'_c(B). \tag{103}$$

Taking difference of these two equations and taking into account the fact that $B \downarrow (p, B_m) = B \uparrow (p, B_a)$, we integrate both sides of the resulting equation from $0 \rightarrow p$ to obtain :

$$\begin{aligned}
& \frac{\partial B_a}{\partial p} = \exp(-B_a / B_r) \\
& \times \left\{ 2 \frac{\partial B \downarrow (p, B_m)}{\partial p} \exp(B \downarrow (p, B_m) / B_r) \right. \\
& \left. \times \left[\exp\left(\frac{H_1^* p}{B_r a}\right) \Theta(B_0 - B_a) \right. \right. \\
& \left. \left. + \exp\left(\frac{H_2^* p}{B_r a}\right) \Theta(B_a - B_0) \right] \right\}.
\end{aligned} \tag{104}$$

Now, if the starting field $B_m > B_0$, integrating both sides of the above equation from $0 \rightarrow p$, we obtain :

$$\begin{aligned}
& \exp(B_a / B_r) = \exp(B_m / B_r) + 2 \\
& \left[\exp\left((H_1^* p + B \downarrow (p, B_m)) / B_r\right) - \right. \\
& \left. \frac{H_1^*}{B_r} \int_0^p dp \exp\left((H_1^* p + B \downarrow (p, B_m)) / B_r\right) \right].
\end{aligned} \tag{105}$$

In the third region $x > p + \delta p$, the field profile is similar to the field decreasing envelope.

(d) *Reversal from the field increasing envelope :*

In a similar manner, for reversal at a field value B_m from the field increasing envelope, in the first region $0 < x < p$, the evolution of profiles is governed by the eq. (94) with a positive sign. In the next one, $p < x < p + \delta p$,

$$\partial B \uparrow (x, B_m) / \partial x = -\mu_0 J_c(B) \tag{106}$$

and

$$\partial B \downarrow (x, B_a - \delta B_a) / \partial x = \pm \mu_0 J'_c(B). \tag{107}$$

Taking difference of these two equations and taking into account the fact that $B \uparrow (p, B_m) = B \downarrow (p, B_a)$, we integrate both sides of the resulting equation from $0 \rightarrow p$ to obtain :

$$\begin{aligned}
& \frac{\partial B_a}{\partial p} = \exp(B_a / B_r) \\
& \times \left\{ 2 \frac{\partial B \uparrow (p, B_m)}{\partial p} \exp(-B \uparrow (p, B_m) / B_r) \right. \\
& \left. \times \left[\exp\left(\frac{H_1^* p}{B_r a}\right) \Theta(B_0 - B_a) \right. \right. \\
& \left. \left. + \exp\left(\frac{H_2^* p}{B_r a}\right) \Theta(B_a - B_0) \right] \right\}.
\end{aligned} \tag{108}$$

Now, if the starting field $B_m < B_0$, integrating both sides of the above equation from $0 \rightarrow p$, we obtain :

$$\begin{aligned}
& \exp(-B_a / B_r) = -\exp(-B_m / B_r) + 2 \\
& \left[\exp\left((H_1^* p - B \uparrow (p, B_m)) / B_r\right) \right. \\
& \left. - \frac{H_1^*}{B_r} \int_0^p dp \exp\left((H_1^* p + B \uparrow (p, B_m)) / B_r\right) \right].
\end{aligned} \tag{109}$$

In the third region $x > p + \delta p$, the field profile is similar to the field increasing envelope.

For this simple step function type behaviour of the critical current density, the magnetization envelope curves as well as the minor loops calculated using eq. (98) are shown in Figure 29. The minor loop behaviour is exactly

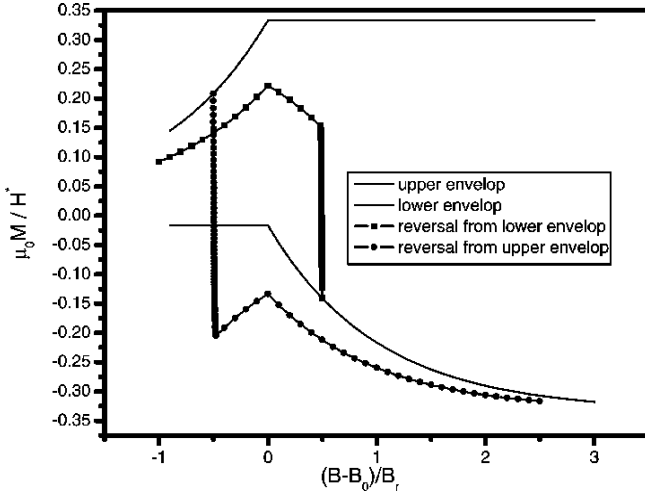


Figure 29. Normalized magnetization curves on the forward and reverse field cycles. The minor loop behaviour exactly matches with those obtained at the high field order-disorder transition regime.

similar to the experimentally observed loops [59,60] at the high field order-disorder transition. All the magnetization curves are plotted with respect to a scaled field $(B - B_0)/B_r$.

6.2.2. Overall characteristics of the order-disorder transitions :

The detailed history dependent features of the low as well as the high field order-disorder transitions (in terms of the minor loop behaviour) can be reproduced by a similar calculation as presented above where the stable current density J^{st} is represented by a double step function or a square well type function (Figure 30) as written symbolically,

$$\begin{aligned} J^{st} &= J_2 \text{ for } B_a < B_1 \text{ and } B_a > B_2, \\ &= J_1 \text{ for } B_1 < B_a < B_2, \end{aligned} \quad (110)$$

or when expressed mathematically,

$$\begin{aligned} J^{st} &= J_1 [\Theta(B_a - B_1) - \Theta(B_a - B_2)] \\ &+ J_2 [\Theta(B_1 - B_a) - \Theta(B_a - B_2)], \end{aligned} \quad (111)$$

assuming $B_2 > B_1$. The upper and the lower envelopes as also the minor loops can be reconstructed for the above current density by employing the earlier results (for a single step function) in an appropriate manner. The detailed description is avoided here. All the experimental features (as listed in the first subsection) of the minor hysteresis loops, both in the low and high field order-disorder transitions, are reproduced by our analytical results. The envelope and minor curves obtained numerically following eq. (97) and the above equations are shown in Figure 31.

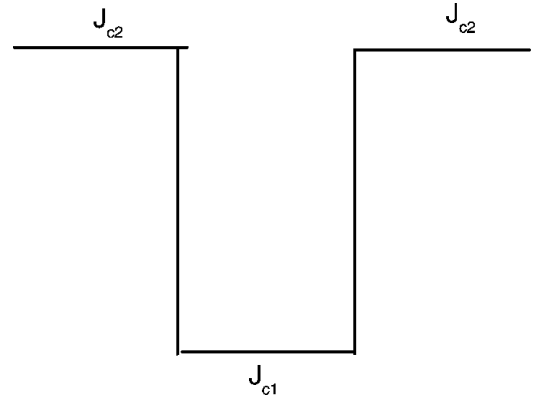


Figure 30. Double-step type (or square-well type) behaviour of the current density representing both the low-field and high-field order-disorder transition.

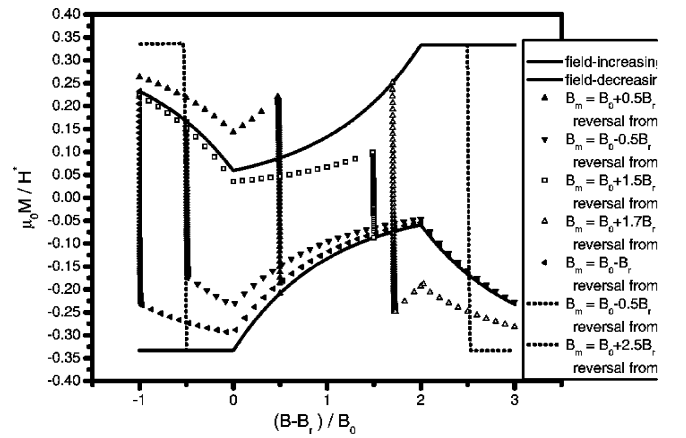


Figure 31. The upper and lower envelopes and the minor curves for the magnetization at the low as well as high field order-disorder transition regimes. The reversal from various points on the upper and the lower envelopes are mentioned in the figure itself.

For an infinite slab geometry, the magnetostriction of the slab is related to the local field by the following expression :

$$\mu_0 S = \frac{1}{a} \int_0^a B^2 dx - B_a^2. \quad (112)$$

The envelope curves as well as the magnetostriction minor loops for weakly pinned systems are shown in Figure 32. The minor loop behaviour is similar as in the magnetization studies.

7. Class III problems

In this section, the response of a hard type-II superconducting disc under quasi-static rotation of the applied magnetic field (see Figure 33) is investigated [60,61]. As mentioned earlier, this belongs to a class III problem.

The dynamics of an array of parallel flux tubes, in a disc of a hard type-II superconductor when subjected to

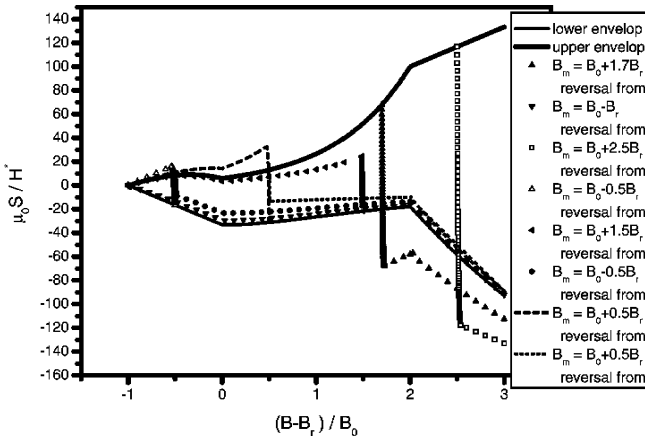


Figure 32. The upper and lower envelopes and the minor curves for the magnetostriction at the low as well as high field order-disorder transition regimes. The reversal from various points on the upper and the lower envelopes are mentioned in the figure itself.

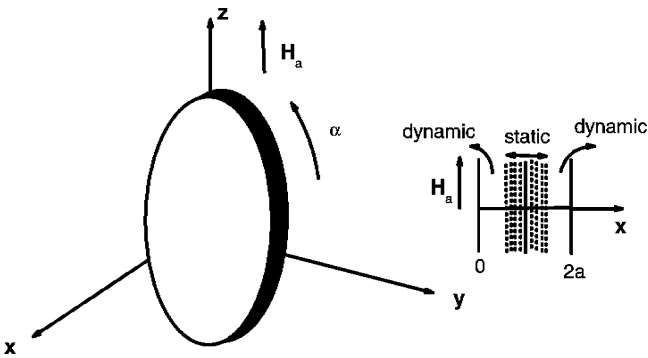


Figure 33. Schematic diagram showing the disc in y - z plane with the field rotating parallel to the face of the disc. The initial applied field direction and the sense of rotation are also shown. At the inset, the division of the sample volume into static and dynamic region is shown for a disc of thickness $2a$.

a quasi-static rotation, was extensively studied in the experimental works of LeBlanc and coworkers [62]. Obviously, it is easier to rotate the disc rather than rotate the externally applied field. Their works on rotating V, VTi discs [63] as also later on Nb discs [64] revealed some very interesting fundamental behaviour of vortex lattice in hard type-II superconductors. Irrespective of the initial magnetic history of the specimen, some general characteristics of flux-lines were observed. This general behaviour also depends on whether the magnitude of the applied field (H_a) is smaller or greater than the full penetration value (H^*) of the field, corresponding to the state when the zero of the internal field profile reaches the midplane of the disk. When $H_a < H^*$, for all initial profiles, the flux density profile remains in a **diamagnetic critical state** near the surface, referred to as the *shoulder* of the $|B|$ profile [64], implying the expulsion of the vortices against Lorentz force. With further rotation, an

almost stable configuration arises where the sample volume is divided into two regions. First, the *stationary* trapped flux region spreading near the midplane, where the vortices remain parallel to the initial applied field direction. In this region, flux lines are rigidly rotating in phase with the disc, retaining their initial orientation. A second region appears adjacent to the surface, where the flux lines gradually change their orientation from zero on the sample surface to a maximum value at the boundary between static and dynamic region. This maximum relative orientation of flux lines with respect to the applied field orientation is referred as the critical angle θ_c in Ref. [64] for a given orientation of the applied field. Once this configuration is achieved, further rotation can not change this situation drastically. In this *active* or *dynamic* region, vortices move relative to the sample and hence energy dissipation occurs due to flux-cutting [65]. There is no energy dissipation in the first or *static* region. When $H_a > H^*$, *dynamic* region spreads within the whole volume and there is no *static* region. LeBlanc *et al* [64] explained their experimental results by using a simple empirical rule relating the spatial distribution of local flux density B and that of the relative orientation ψ of the local B . They assumed that the flux density gradient ($d|B|/dx$) is the same for both the parallel (*static*) and non-parallel (*dynamic*) flux-lines. LeBlanc *et al* calculated the magnetization and other related properties by assuming a linear form for the pinning force. Their assumption of constant flux density gradient is at variance with the theoretical development of Bean [66]. Bean's treatment for the rotating field implies that at the boundary between the *static* and *dynamic* region, the phase lag between the applied field and the local flux density approaches infinity. Due to such discontinuity in the orientation of flux lines in static and dynamic regions, assumption of linear form of pinning force could not explain all of their experimental data. Bean's treatment is also based on the assumption, $\mathbf{J} \times \mathbf{E} = 0$, which is not applicable in the *dynamic* region. Our formulation of finding out the flux-density profiles and other related quantities of interest for a rotating disc, without any such assumption, produce results matching well with the experimental datas of LeBlanc *et al* [64].

In this context, one may mention about the studies of Clem and Pérez-González [65], presenting a phenomenological model describing flux-cutting and rotating field phenomena in great detail. According to their Double Critical State Model (DCSM), the current

density in the *dynamic* region, in response to non-parallel local induction, is along any general direction. The components of the current density parallel and perpendicular to the local magnetic induction have the critical values J_c^{\parallel} and J_c^{\perp} , related to the onset of flux-cutting and to the depinning threshold (onset of flux-flow), respectively. The metastable stationary distribution of local magnetic induction \mathbf{B} is determined by Maxwell equations with the critical state conditions, $|\mathbf{J}_{\perp}| \leq J_c^{\perp}(\mathbf{B})$ and $|\mathbf{J}_{\parallel}| \leq J_c^{\parallel}(\mathbf{B})$. The latter inequality of parallel component can be rewritten in terms of the gradient of the critical angle [65]. Clem *et al* [65] have considered samples with different magnetic history and shown how under rotation, the sample volume is divided into different zones, where different phenomena like flux-cutting or flux-transport occur individually or coexist.

Badía and López [21] have also addressed the problem of rotating field by using their Optimal Control Model (OCM) to determine the field profiles. The method involves successive use of the procedure where the new profile \mathbf{H}_{n+1} is obtained by minimizing the functional $C[\mathbf{H}_{n+1}(x)]$ related with the finite difference between the $(n + 1)$ -th and n -th profile integrated over the volume of interest. This approach is very similar to the one discussed in Ref. [5] and has been followed here [60,61]. In their work, the authors have chosen a sample with a non-magnetic initial profile and have reproduced experimental features pertaining to this case. Recently, they have used the same technique [48] to detail the critical state behaviour under rotation, with anisotropic critical current density.

In the present study, we consider the problem of a hard type-II superconductor disc subjected to a rotating magnetic field of constant magnitude. As mentioned in Refs. [21,5], Bean's original statement of Critical State Model (CSM) does not unambiguously lead to the final solution when the change in the applied field is in a direction different from that of the initial field. The non-uniqueness of local field profiles is resolved by imposing an additional criterion of minimum flux-change. This criterion enables us to determine uniquely the final metastable state from the various accessible ones. Here, we describe the formulation of the problem by defining a variational functional representing the measure of the change of the flux within the sample. Final results are obtained by a self-consistent solution of the resulting equations. Using this methodology, we obtain the field

profiles and magnetization for three initial profiles, *viz.* non-magnetic, diamagnetic and paramagnetic with *isotropic* and *field-independent* J_c . With gradual rotation of the field, the evolution of the profiles for $|\mathbf{B}|$ and the y and z components are studied starting from an initial profile. The angle of orientation ψ of the local field \mathbf{B} within the sample is determined as a function of distance from the midplane of the disc. Other quantities of interest such as critical angle, the location of the decoupling point *etc.* are studied as a function of magnitude of the applied field for typical angles of rotation. Components of magnetization and average local field are also determined from the field profiles. Our results compare well with earlier experimental results.

In this study, we do not include anisotropy in J_c , this being our first non-trivial application of the minimum flux-change technique. The effects of anisotropy and field dependence in J_c can be included without major modifications in the procedure. This can be done as a next step to this isotropic J_c case.

7.1. Formulation :

Let us assume that the field is rotating in the $y - z$ plane with the x -axis as its axis of rotation. Initially, let the magnetic field be applied along z -direction. In Figure 32, we have shown schematically the sample geometry.

Under the approximation that, diameter of the disc is much greater than its thickness, the dimensionality of the problem reduces to one. The quantity related to the change of flux within the sample is $\int |\delta B(x)|^2 dx$ [5]. If the initial profile is given by $B_z = f(x)$ and $B_y = g(x)$, one can define the variational functional $Q[J]$ as :

$$Q[J] = \int \left\{ [B_z - f(x)]^2 + [B_y - g(x)]^2 \right\} dx \quad (113)$$

representing the measure of the change of flux within the sample. We have to solve Maxwell's equation $\Delta \times \mathbf{B} = \mu_0 \mathbf{J}$, which for this particular geometry, reduces to the following partial differential equations :

$$\partial B_z / \partial x = -\mu_0 J_y, \quad \partial B_y / \partial x = \mu_0 J_z. \quad (114)$$

The field components $B_z(x)$ and $B_y(x)$ are determined from the above eqs. (114) starting from the initial profiles by minimizing the functional Q with respect to the change of current distribution, subject to the constraint $J_y^2 + J_z^2 = J_c^2$. The solutions of eq. (114) can be written as :

$$B_z(x) = B_z(a) + \mu_0 \int_x^a J_y(u) du, \quad (115)$$

$$B_y(x) = B_y(a) - \mu_0 \int_x^a J_z(u) du, \quad (116)$$

where $2a$ is the thickness of the disc. For the case of rotating field of magnitude B_0 , $B_z(a) = B_0 \cos \alpha$ and $B_y(a) = B_0 \sin \alpha$. Substituting for B_z and B_y from eqs. (115) and (116) into (113) and minimizing Q with respect to variation in \mathbf{J} we get equations that determine the components of current density in terms of auxiliary quantities I_y and I_z :

$$J_z = J_c I_y / I, \quad J_y = -J_c I_z / I, \quad I = (I_y^2 + I_z^2)^{1/2}, \quad (117)$$

where

$$I_y(x) = \int_0^x \{B_y(u) - g(u)\} du, \quad (118)$$

$$I_z(x) = \int_0^x \{B_z(u) - f(u)\} du. \quad (119)$$

Eqs. [(115)–(119)] must be solved self consistently to get the final profile. Starting with the given initial profile, we have determined the successive profiles by an iterative process taking the profile at any stage as the initial profile for the next stage. This aspect is discussed in greater detail in the next section.

7.2. Evolution of profiles :

We have considered three different possible magnetic histories for the sample *viz.* non-magnetic, diamagnetic and paramagnetic. The non-magnetic case is presented in detail. Details of features for the other two cases which are similar to the non-magnetic case are only briefly presented. The numerical solution of eqs. (115)–(119) is obtained by following an iterative procedure. We now discuss the evolution of field profiles for the three initial profiles.

7.2.1. Non-magnetic initial profile :

For this case, initially the field is along z -direction and its magnitude is constant throughout the sample, *i.e.* $B_z(x) = B_0$, $B_y(x) = 0$. Realistically, this situation can be achieved when a zero field cooled sample with negligible pinning is subjected to a field beyond the field corresponding to full penetration. With gradual rotation of the field, the profiles for $|\mathbf{B}|$, B_y , B_z and the angle of orientation of the local \mathbf{B} are plotted as functions of position x in Figure 34. Figure 34(a) depicts the variation of flux-density modulus with x for α varying from 0 to

2π at a step size of 10° . With increase of α , the area under the trough shaped profile (in the dynamic region) gradually increases. In Figure 34, the evolution of the profiles with the increase of α is denoted by an arrow in the figures.

During initial changes of α , flux density modulus decreases near the surface in the *dynamic* region and with further rotation the trough region evolves into a ‘V’ shape with rounded tip. With continued rotation, for a particular α -value, the tip of this ‘V’ becomes sharp and touches $|\mathbf{B}| = 0$ line at a point X_0 indicating a slope discontinuity in $|\mathbf{B}(x)|$ profile at X_0 , referred to as the *decoupling point* [21] for the non-magnetic initial profile.

The development of $|\mathbf{B}|$ curve into a ‘V’ shape can be understood in the following way. Using $B_z = |\mathbf{B}| \cos \psi$ and $B_y = |\mathbf{B}| \sin \psi$ in eq. (114), we get after some simplification

$$\left(\frac{d|\mathbf{B}|}{dx} \right)^2 + |\mathbf{B}|^2 \left(\frac{d\psi}{dx} \right)^2 = \mu_0^2 J_c^2. \quad (120)$$

Thus J_c is composed of two contributions. Conventionally, $d|\mathbf{B}|/dx$ is identified with $\mu_0 J_\perp$ and $|\mathbf{B}| (d\psi/dx)$ with $\mu_0 J_\parallel$ (eqs. (3) and (4) in Ref. J R Clem, *Phys. Rev.* **B26** 2463 (1982)). However, we do not need to assume the existence of $J_{c\parallel}$ and $J_{c\perp}$ in the present work to obtain the decoupling point. The mere existence of a non-zero J_\parallel ensures flux-cutting. J_\parallel becomes predominant in region where $d|\mathbf{B}|/dx$ (or $|\mathbf{B}|$) is small or $(d\psi/dx)$ is large. Thus, the region in the vicinity of the tip of ‘V’, there is large flux-cutting.

For a given B_0 value, decoupling occurs at a particular angle α_d . In Figure 34, for $B_0 = 0.35B^*$, $\alpha_d = 330^\circ$ and $X_0/a = 0.53$. For rotations beyond α_d , in the region $x < X_0$, the profiles for $|\mathbf{B}|$, B_y and B_z effectively remain unchanged. In Figure 34(b), variation of orientation ψ of the flux tubes are shown. The curve corresponding to decoupling ($\alpha = \alpha_d$), has undergone a discontinuous jump at the decoupling point and thereafter, the variation of orientation near the static region is very small. For $\alpha > \alpha_d$, the nature of discontinuity remains same with the freezing of curves beyond decoupling. The $\psi(x)$ curve for $\alpha = \alpha_d$, where it is first having a discontinuity, is shown as an inset of Figure 34(b), where the jump at X_0 is very obvious. Comparing with Clem *et al* [65] at X_0 , the value of $d\psi/dx$ crosses the value of critical angle gradient, rendering the onset of flux-cutting at X_0 . In Refs. [64], the authors have defined *critical angle* θ_c , as the relative orientation of the flux tubes at X_0 with

respect to the field orientation at the surface. The quantitative definition is given by the expression :

$$\theta_c = \int_1^{X_0} \left(\frac{d\psi}{dx} \right) dx = \psi(X_0) - \alpha. \quad (121)$$

While comparing a similar expression for θ_c in Ref. [64], it should be remembered that in the present case, the

surface is at $x = 1$. It is very obvious from the Figure 34(b) that value of θ_c changes with B_0 as well as with the field orientation α at the surface.

In our study, we follow the definition given in the eq. (121) and have studied the variation of θ_c as a function of B_0 and α . In both of the Figures 34(a) and (b), the boundary of core region denoted as X_c are shown. From

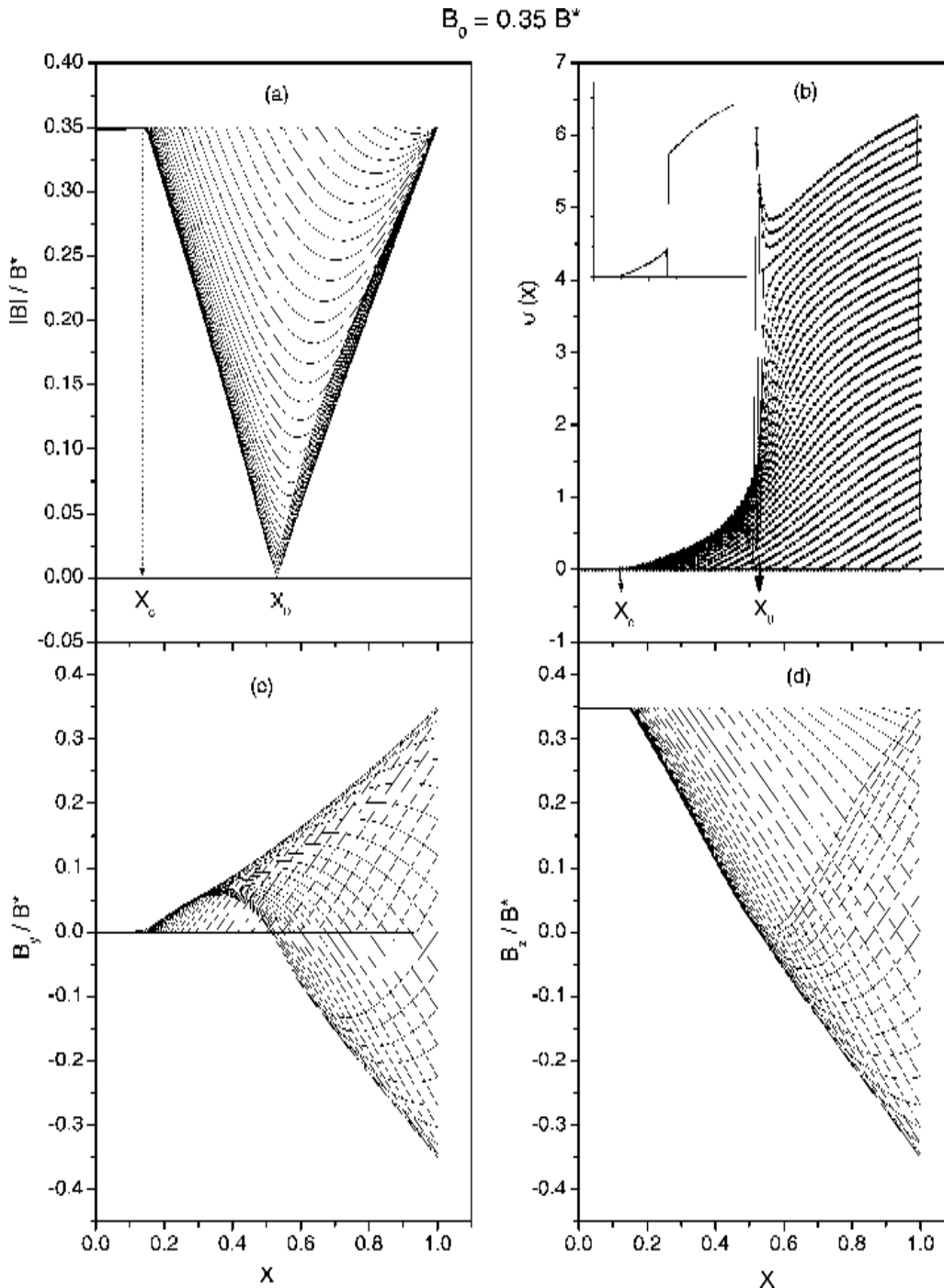


Figure 34. Evolution of field profiles with non-magnetic initial profile. With gradual rotation of the field, the profiles for (a) $|B|$, (b) ψ , the orientation of local B, (c) B_y and (d) B_z , plotted as a function of position x in units of a . The inset in Figure 2(b) depicts the occurrence of decoupling at $\alpha_0 = 330^\circ$. Movement of the profiles with increase in α is denoted by arrows in the figures. The meaning of different arrows is depicted in the corresponding figures.

this point onwards, the final profile coincides with the initial one, rendering the magnitude as well as the direction of the local flux-density to be equal to their initial value.

In Figure 35, we have shown the change in the nature of decoupling with varying B_0 . It is seen that with increasing B_0 , decoupling (discontinuous jump in flux line orientation) occurs at a higher α value, implying that

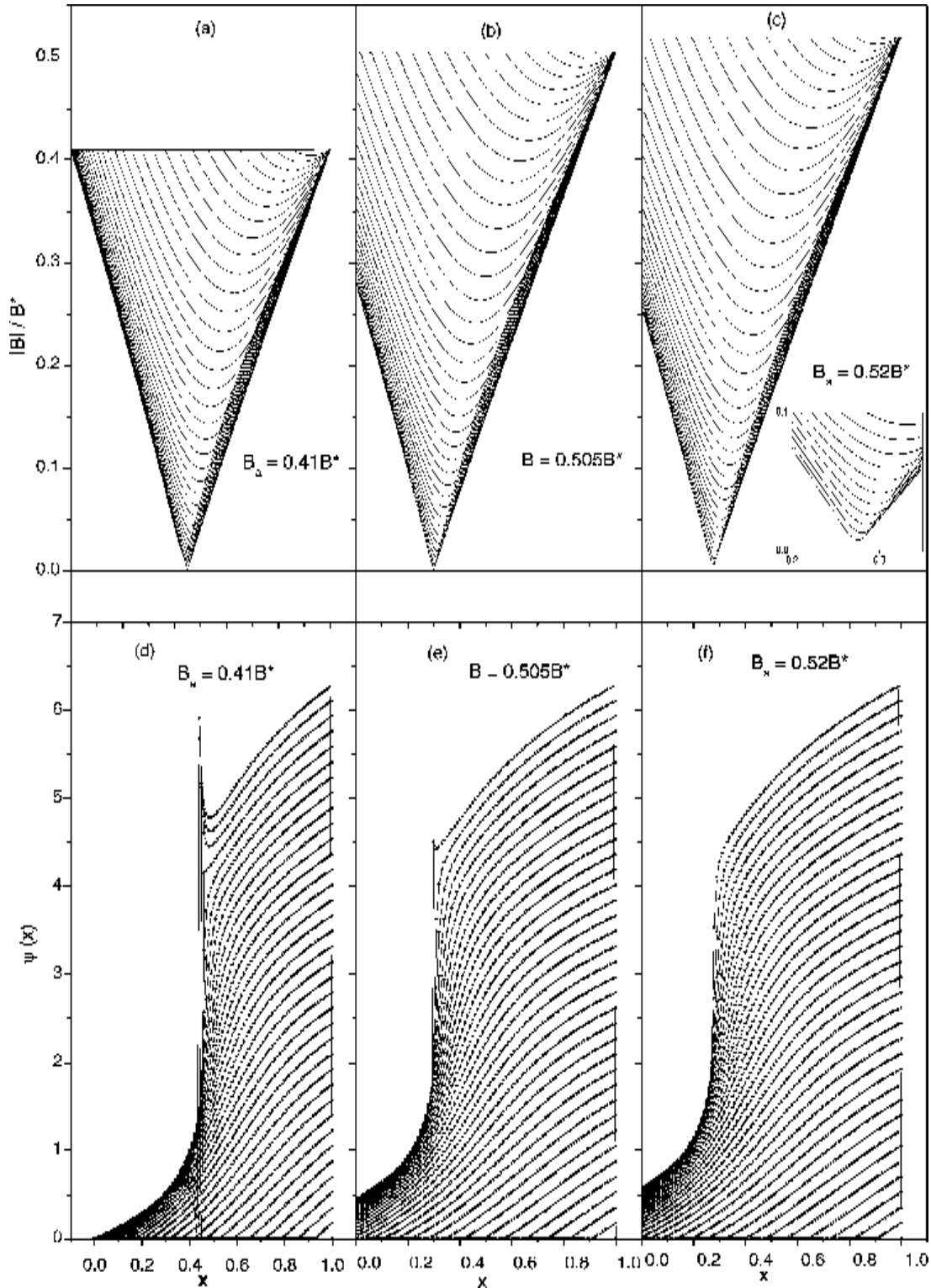


Figure 35. Change in the nature of decoupling for different magnitudes of the applied field, (a) and (d) $|B|$ and ψ profiles for $B_0 = B_p = 0.41B^*$, (b) and (e) for $B_0 = 0.505B^* > B_p$, (c) and (f) for $B_0 = 0.52B^*$ beyond B_p .

if the initial field value is higher, more rotation is required to arrive at a stable profile. With the increase of B_0 , the 'V' shifts towards the midplane. When $X_c = 0$, corresponding to the full penetration value B_p , the profiles for $|B|$ and ψ are shown in Figures 35(a) and (d) for $B_0 = B_p = 0.41B^*$. The profile shows decoupling clearly. With increase of B_0 , α_d becomes higher upto $B_0 = 0.505B^* > B_p$, where decoupling occurs just at $\alpha_d = 2\pi$ (Figures 35(b) and (e)). The last curve of Figure 35(e) clearly shows the discontinuity. With further increase of B_0 , as is obvious from Figures 35(c) and (f), that there is no decoupling upto $\alpha = 2\pi$. From the inset of Figure 35(c), for $B_0 = 0.52B^*$, the separation of the tip of 'V' from the zero field line is clearly seen. With further increase of B_0 , the decoupling point shifts towards the midplane. This process will continue until the tip of the 'V' joins with the midplane, where the decoupling occurs for $\alpha \leq 2\pi$.

In Figure 36(a), we have shown the variation of θ_c as a function of B_0 for different α values. The figure has resemblance with the experimental datas plotted in [64], whereas their theoretical analysis produced a straight line for the same. For small α values, the extent of *core* (*static*) region is less, spread in the variation of ψ is less starting from the surface. Also the jump corresponding to

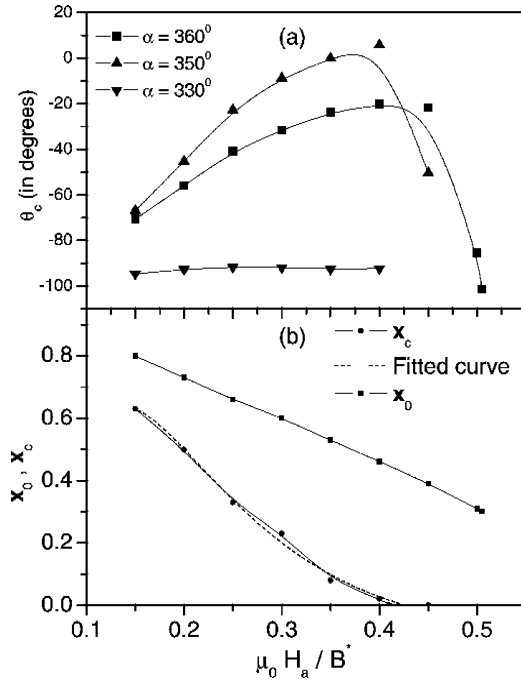


Figure 36. (a) Variation of θ_c as a function of B_0 for three different α values are shown. (b) Variation of decoupling point X_0 and the extent of the core region X_c with B_0 is shown. The dotted curve represents third order exponential decay fit to the X_c curve.

X_0 is less. The flux lines mostly try to retain their initial direction. The *dynamic* region effectively acts as a shielding to the external change of orientation and hence prevents the *core* flux tubes to follow the external orientation. With increase of the field upto B_p , the shielding becomes gradually less effective, allowing the core to orient more towards the surface field orientation. At $B_0 = B_p$, $X_c = 0$, there is a maxima in the θ_c vs B_0 curve, implying that all the flux lines are maximally oriented towards the surface field direction. With further increase of the field, again θ_c decreases, shielding becomes again more effective, rendering the flux lines to retain their initial orientation. The tendency of retaining the initial orientation is even stronger in the high field region, due to more effective shielding of the *dynamic* region, than in the low field region. A comparison of Figures 35(a) and (b) for lower and higher B_0 supports this fact. Figure 36(b) shows the variation of X_0 and X_c with the applied field. The former is having a linear behaviour, whereas latter is varying almost exponentially with the applied field. We have fitted the X_c vs B_0 curve with a third order exponential decay as shown in Figure 35(b). The functional form is given by $X_c = a_1 \exp(-B_0/t_1) + a_2 \exp(-B_0/t_2) + a_3 \exp(-B_0/t_3)$, with required parameter values given by $a_1 = 4.47817$, $t_1 = 0.11697$, $a_2 = -8.41008$, $t_2 = 0.05307$, $a_3 = -0.11457$, $t_3 = -1.9279$ with $\chi^2 = 0.00067$ and $R = 0.9964$. Given an initial applied field value, by using the above formula, one can find out the extension of the core (*static*) region.

7.2.2. Diamagnetic initial profile :

The initial profile is given by $B_z(x) = B_0 - (1 - x)$ for $x \geq x_p$, $B_z(x) = 0$ otherwise. $B_y(x) = 0$ for all x . Here, $B_0 = (1 - x_p)$ with x_p being the maximum extent of penetration in the initial state. The initial profile has resemblance with field increasing profiles for a zero-field-cooled (ZFC) sample. With gradual changes of α , the profiles for $|B|$, B_y , B_z and orientation of local B are plotted as a function of position x in Figure 37 upto $\alpha = 250^\circ$ at a step size of 10° for $B_0 = 0.3B^*$.

From Figure 37(a), it is evident that near the surface, there exists a dynamic region in a diamagnetic critical state, where the slope of the $|B|$ profile is gradually increasing and after a certain value of α , it evolves into a 'V' shaped profile with unequal hands and rounded tip. This process will continue until decoupling occurs at $\alpha = \alpha_d = 230^\circ$, where the tip of 'V' touches $|B| = 0$ line at $x = X_0$, the *decoupling point* for the diamagnetic initial

profile. For $x < X_0$, and $\alpha > \alpha_d$, all the profiles essentially remain the same as at $\alpha = \alpha_d$. As in the non-magnetic profile, the $\psi(x)$ profile in the present case, has also shown the first discontinuous jump for $\alpha = \alpha_d$ corresponding to $x = X_0$ in Figure 37(b). All the other features remain similar to those of the non-magnetic case.

Regarding the minimization procedure, there are interesting results to be pointed out. We have obtained the evolution of the profiles by carrying out the minimization, considering the previous profile as the initial profile. Instead of the above procedure, if the minimization is done with respect to the very first profile,

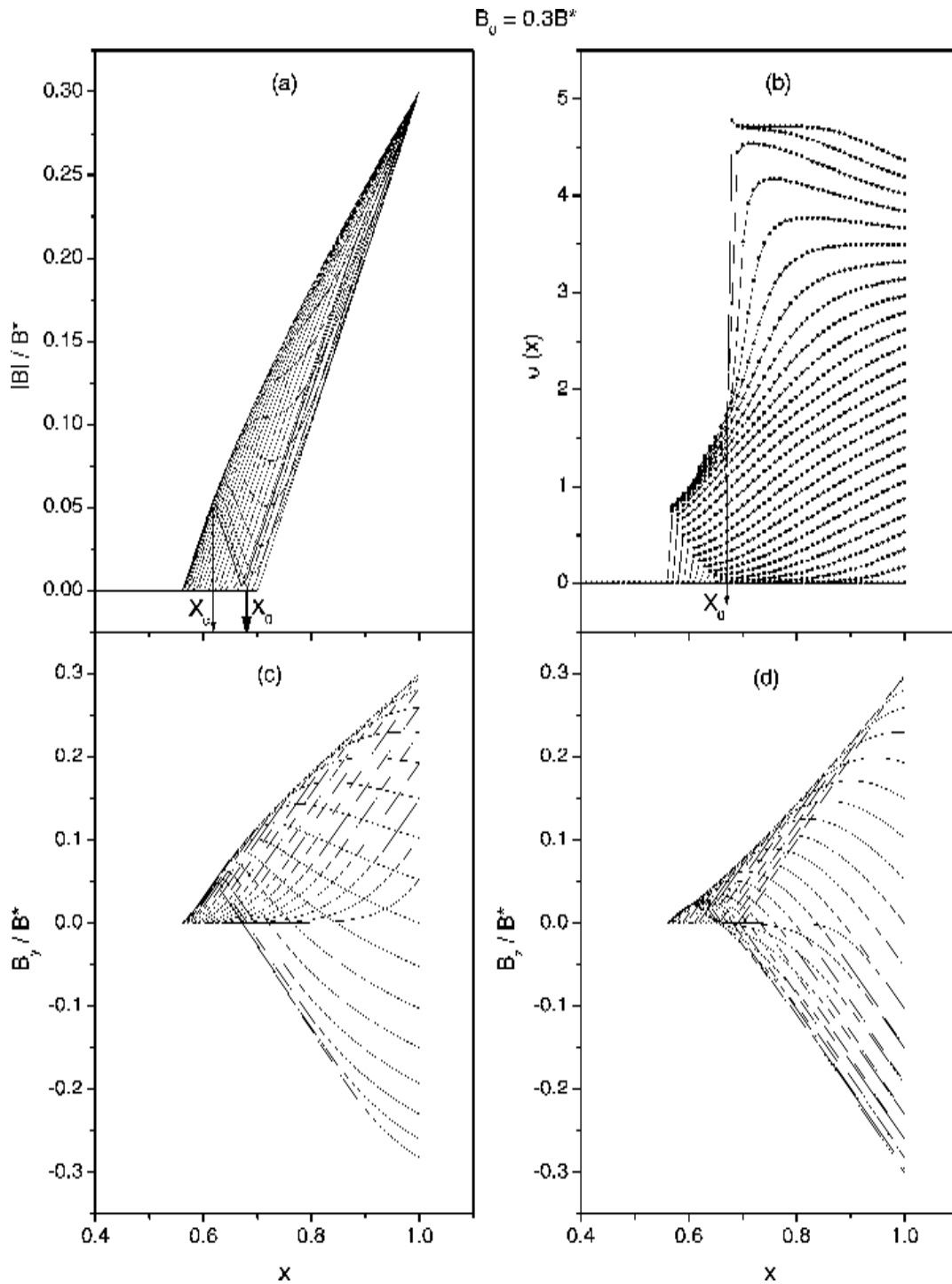


Figure 37. Evolution of field profiles with diamagnetic initial profile. With gradual rotation of the field, the profiles for (a) $|B|$, (b) orientation ψ of local B , (c) B_y , and (d) B_z are plotted as a function of position x in units of a . The profiles are obtained considering the previous profile as the initial profile.

the evolution obtained shows some different nature, especially for the $\psi(x)$ profile. Physically, the minimization procedure can be viewed as, each time after a certain change of α , the disc again is brought back to the $\alpha = 0^\circ$ position. The corresponding profiles are shown in Ref. [60] upto $\alpha = 180^\circ$. These profiles show decoupling at a much lower α value alongwith the vanishing of the peak before a discontinuous jump in $\psi(x)$.

7.2.3. Paramagnetic initial profile :

The initial profile is given by, $B_z(x) = B_0 + (1 - x)$, $B_y(x) = 0$ for all x . This initial profile is similar to the field reversal profiles for a ZFC sample beyond full penetration. With gradual changes of α , the profiles for $|B|$, B_y , B_z and orientation of local B are plotted as a function of position in Figure 38 upto $\alpha = 250^\circ$ at a step size of 10° for $B_0 = 0.4B^*$. Similar to the other two studied cases, in

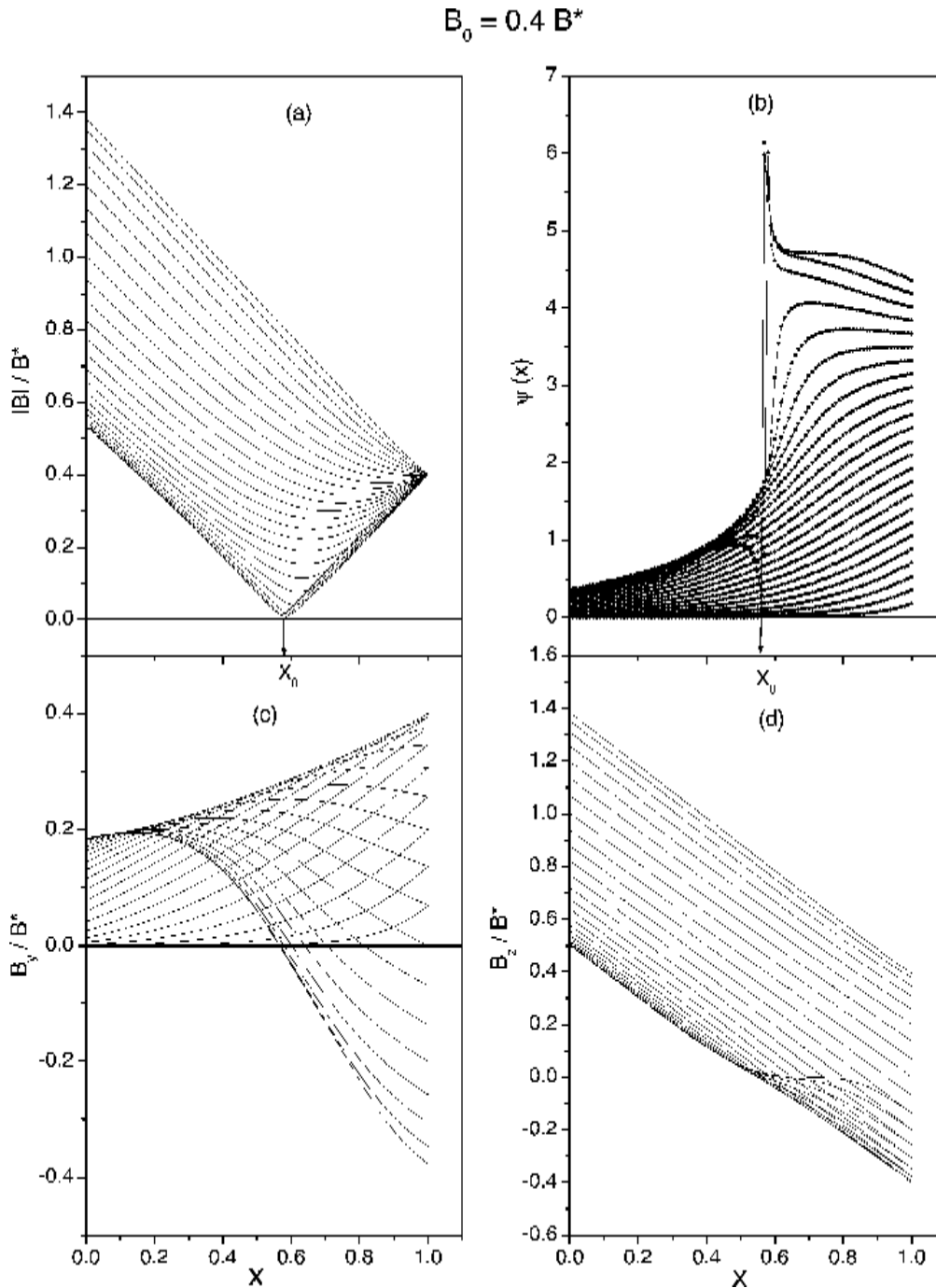


Figure 38. Evolution of field profiles with paramagnetic initial profile. With gradual rotation of the field, the profiles for (a) $|B|$, (b) orientation of local B , (c) B_y and (d) B_z are plotted as a function of position x in units of a . The profiles are obtained considering the previous profile as the initial profile.

the dynamic region, the sample remains in the diamagnetic critical state with slope of the profiles gradually increasing. This profile shows decoupling at $\alpha = \alpha_d$ corresponding to $x = X_0$ as shown in Figures 38(a) and (b).

All the other features remain the same as for the other two studied cases. The evolution of the profiles following the other minimization technique, where after each step, the orientation of the field is brought back to zero, is again presented in [60]. As earlier, the $\psi(x)$ curve shows a definite change.

In Figure 39, we have plotted the y and z components of magnetization and the respective components of average field with respect to α varying upto 250° for samples having different magnetic history as mentioned previously. These curves show a general agreement with those reported by [63].

For studying the behaviour of the field profiles, we had to choose appropriate magnitude of the applied field in order to capture the onset of decoupling with the fixed step size of 10° . For diamagnetic and paramagnetic cases, the profiles were plotted upto a few steps beyond decoupling was obtained.

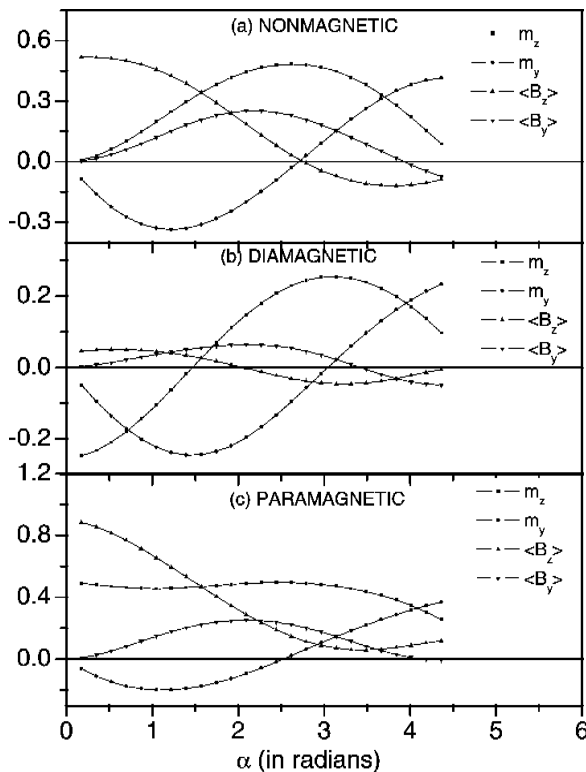


Figure 39. Shows y and z components of magnetization and the respective components of average field as functions of α varying upto 250° for samples having different magnetic histories as (a) non-magnetic, (b) diamagnetic, (c) paramagnetic.

7.3. Summary

We have analysed the problem of a sample with isotropic critical current density and zero demagnetization factor subjected to a rotating magnetic field. To get a unique solution to the CSM, the criterion of minimum change of flux was employed. The profiles for the components of the local field, its orientation angle and also its magnitude are obtained. Some of the known general features associated with this problem such as the decoupling, variation of the critical angle with the change of the magnitude of the applied field could be reproduced. Thus the procedure invoking minimum flux change criterion, followed here, should be useful for solving other similar critical state problems which include field dependence and anisotropy in the critical current density.

8. Conclusions

We have categorized the possible sample geometries and presented the solutions of some realistic problems belonging to all these three classes. We have also discussed their applications for various purposes to analyse the experimental data. Our results also resembles well with the experimental results.

Acknowledgments

The author is grateful to Late Dr. K V Bhagwat and Prof. G P Das for useful discussions.

References

- [1] C P Bean *Rev. Mod. Phys.* **36** 31 (1964)
- [2] Charles P Poole (Jr.), Horacio A Farach and Richard J Creswick *Superconductivity* (New York : Academic Press) (1988)
- [3] C P Bean *Phys. Rev. Lett.* **8** 250 (1962)
- [4] R P Huebner *Magnetic Flux Structures in Superconductors* (New York : Springer) (1979)
- [5] K V Bhagwat, S V Nair and P Chaddah *Physica* **C227** 176 (1994)
- [6] J R Clem in : *Magnetic Susceptibility of Superconductors and Other Spin Systems* (eds) R A Hein, T L Francavilla and D H Leibengerg (New York : Plenum) p177 (1992)
- [7] Y Kato, M Hanakawa and K Yamafuji *Jpn. J. Appl. Phys.*, **15** 695 (1976)
- [8] M N Wilson *Superconducting Magnets* (Oxford : Clarendon Press) (1963)
- [9] P N Mikheenkov and Yu E Kuzovlev *Physica* **C204** 229 (1993)
- [10] E H Brandt and M Indenbom *Phys. Rev.* **B48** 12893 (1993)
- [11] J Mc Donald and J R Clem *Phys. Rev.* **B53** 8643 (1996) and references therein
- [12] K V Bhagwat and P Chaddah *Physica* **C280** 52 (1997)
- [13] D V Shantsev, Y M Galperin and T H Hohansen *Phys. Rev.* **B60** 13112 (1999)

- [14] K V Bhagwat and P Chaddah *Pramana-J. Phys.* **33** 521 (1989); *Physica* **C224** 155 (1994)
- [15] K V Bhagwat and P Chaddah *Physica* **C190** 444 (1992)
- [16] R Navarro and L J Campbell *Phys. Rev.* **B44** 10146 (1991)
- [17] L Prigozhin *J. Comp. Phys.* **129** 190 (1996)
- [18] M Ashkin *J. Appl. Phys.* **50** 7060 (1979)
- [19] K L Telchow and Koo *Phys. Rev.* **B50** 6923 (1994)
- [20] E H Brandt *Phys. Rev.* **B58** 6506 (1998)
- [21] A Badía and C López *Phys. Rev. Lett.* **87** 127004 (2001)
- [22] K V Bhagwat and D Karmakar *Pramana-J. Phys.* **57** 763 (2001)
- [23] Debjani Karmakar and K V Bhagwat *Pramana-J. Phys.* **56** L127 (2000)
- [24] Debjani Karmakar and K V Bhagwat *Phys. Rev.* **B65** 024518 (2001)
- [25] D Karmakar and K V Bhagwat *Physica* **C398** 20 (2003)
- [26] K V Bhagwat and D Karmakar *Europhys. Lett.* **49** 715 (2000)
- [27] N I Muskhelishvili *Singular Integral Equations* (Groningen-Holland : Noordoff) (1953)
- [28] A Perez-Gonzalez and J R Clem *Phys. Rev.* **B42** 4100 (1990) and references therein.
- [29] L Biberbach *Conformal Mapping* (translated by F Steinhardt) (New York : Chelsea) (1953)
- [30] Yu E Kuzovlev *JETP Lett.* **61** 1000 (1995)
- [31] Th. Wolf, A-C. Bornarel, H Kupfer, R Meier-Hirmer and B Obst *Phys. Rev.* **B56** 6308 (1997)
- [32] Debjani Karmakar and K V Bhagwat *Proceedings of DAE Solid State Physics Symposium* **45** 405 (2002)
- [33] F Gömöry *Supercond. Sci. Technol.* **10** 523 (1997)
- [34] A M Campbell *J. Phys.* **C2** 1492 (1969)
- [35] J R Clem *Physica* **C153-155** 50 (1988)
- [36] Y J Zhang and C K Ong *Appl. Phys. Lett.* **79** 509 (2001)
- [37] C Senatore, M Polichetti, N Clayton, R Flükiger and S Pace *Physica* **401** 182 (2004)
- [38] E H Brandt *Phys. Rev.* **B58** 6523 (1998)
- [39] Debjani Karmakar *accepted in Physica C* (2005)
- [40] Debjani Karmakar and K V Bhagwat *Proceedings of DAE Solid State Physics Symposium* (Chandigarh) **46** 831 (2003)
- [41] K V Bhagwat, Debjani Karmakar and G Ravikumar *J. Phys. : Condens. Matter* **15** 1325 (2003)
- [42] A M Campbell and J E Evetts *Adv. Phys.* **21** 199 (1972)
- [43] K V Bhagwat and P Chaddah *Physica* **C280** 52 (1997)
- [44] R Navarro and L J Campbell *Phys. Rev.* **B44** 10146 (1991)
- [45] E H Brandt *Phys. Rev.* **B54** 4246 (1996)
- [46] H. Küpfer, G Ravikumar, Th. Wolf, A A Zhukov, A Will, H Leibrock, R Meier-Hirmer, H Wühl and P A J de Groot *Phys. Rev.* **B66** 064512 (2002)
- [47] Shashwati Sen, A Singh, D K Aswal, S K Gupta, J V Yakhmi, V C Sahni, E- M Choi, H-J Kim, K H P Kim, H-S Lee, W N Kang and S-I Lee *Phys. Rev.* **B65** 214521 (2002)
- [48] Th. Schuster, H Kuhn, E H Brandt and S Klaumünzer *Phys. Rev.* **B56** 3413 (1997)
- [49] A Badia and C López *arXiv : cond-mat/0209494* v1 (20 Sep 2002)
- [50] K V Bhagwat and P Chaddah *Phys. Rev.* **B44** 6950 (1991-I)
- [51] I N Sneddon *Elements of Partial Differential Equations* (New York : McGraw-Hill) p59 (1957)
- [52] G P Mikitik and E H Brandt *Phys. Rev.* **B62** 6812 (2000-II)
- [53] Y Paltiel, E Zeldov, Y N Myasoedov, H Shtrikman, S Bhattacharya, M J Higgins, Z L Xiao, E Y Andrei, P L Gammel and D J Bishop *Nature* (London) **403** 398 (2000)
- [54] G Ravikumar, H. Küpfer, A Will, R Meier-Hirmer and Th. Wolf *Phys. Rev.* **B65** 094507 (2002) and references therein
- [55] A I Larkin and Y N Ovchinnikov *Zh. Èksp. Teor. Fiz.* **65** 1704 (1973) [*Sov. Phys. JETP* **38** 854 (1974)]
- [56] Gautam I Menon *Phys. Rev.* **B65** 104527 (2002)
- [57] D G Kulkarni, M R Singh, D Karmakar, T V Chandrasekhar Rao, P K Mishra, G Ravikumar, K V Bhagwat and H Küpfer *Physica* **C385** 178 (2003)
- [58] G Ravikumar, K V Bhagwat, V C Sahni, A K Grover, S Ramakrishnan and S Bhattacharya *Phys. Rev.* **B61** R6479 (2000)
- [59] G Ravikumar, V C Sahni, A K Grover, S Ramakrishnan, P L Gammel, D J Bishop, E Bucher, M J Higgins and S Bhattacharya *Phys. Rev.* **B63** 024505 (2000)
- [60] D Karmakar and K V Bhagwat *Physica* **C406** 210 (2004)
- [61] D Karmakar and K V Bhagwat *Proceedings DAE Solid State Physics Symposium* (Chandigarh) **46** (2002)
- [62] R Boyer and M A R LeBlanc *Solid State Commun.* **24** 261 (1977)
- [63] R Boyer, G Fillion and M A R LeBlanc *J. Appl. Phys.* **51** 1692 (1980)
- [64] J R Cave and M A R LeBlanc *J. Appl. Phys.* **53** 1631 (1982)
- [65] J R Clem *Phys. Rev.* **B26** 2463 (1982); J R Clem and A Pérez-González *Phys. Rev.* **B30** 5041 (1984); A. Pérez-González and J R Clem *Phys. Rev.* **B31** 7048 (1985); *J. Appl. Phys.* **58** 4326 (1985)
- [66] C P Bean *J. Appl. Phys.* **41** 2482 (1970)

About the Reviewer

Dr. Debjani Karmakar obtained her Ph.D. Degree in 2005 from University of Mumbai and is currently working as a Scientific Officer at Bhabha Atomic Research Centre, Mumbai. Her Fields of interest are :

- (a) Applied Superconductivity : (Analytical calculations for various magnetization properties of hard type-II superconductors) and
- (b) Magnetic Materials : First-principles investigation of transition metal doped oxides.

She is a recipient of IPS Young Physicist Award (2002) and has published a number of papers in reputed journals.